DESIGN, CONSTRUCTION AND IMPLEMENTATION OF SPHERICAL TISSUE EQUIVALENT PROPORTIONAL COUNTER

A Dissertation

by

DELIA PEREZ NUNEZ

Submitted to the Office of Graduate Studies of
Texas A&M University
in partial fulfillment of the requirements for the degree of

DOCTOR OF PHILOSOPHY

May 2008

Major Subject: Nuclear Engineering

DESIGN, CONSTRUCTION AND IMPLEMENTATION OF SPHERICAL TISSUE EQUIVALENT PROPORTIONAL COUNTER

A Dissertation

by

DELIA PEREZ NUNEZ

Submitted to the Office of Graduate Studies of
Texas A&M University
in partial fulfillment of the requirements for the degree of

DOCTOR OF PHILOSOPHY

Approved by:

Co-Chairs of Committee,	Leslie A. Braby
	John Ford
Committee Members,	John W. Poston, Sr.
	William S. Charlton
	Rainer Fink
Head of Department,	Raymond Juzaitis

May 2008

Major Subject: Nuclear Engineering

ABSTRACT

Design, Construction and Implementation of Spherical Tissue Equivalent Proportional Counter.

(May 2008)

Delia Perez Nunez, B.S., Universidad Central de Venezuela

Co-Chairs of Advisory Committee: Dr. Leslie A. Braby
Dr. John Ford

Tissue equivalent proportional counters (TEPC) are used for medical and space activities whenever a combination of high and low LET (lineal energy transfer) radiations are present. With the frequency and duration of space activities increasing, exposure to fast heavy ions from galactic cosmic radiation and solar events is a major concern. The optimum detector geometry is spherical; to obtain an isotropic response, but simple spherical detectors have the disadvantage of a non-uniform electric field. In order to achieve a uniform electric field along the detector axis, spherical tissue equivalent proportional counters have been designed with different structures to modify the electric field. Some detectors use a cylindrical coil that is coaxial with the anode, but they are not reliable because of their sensitivity to microphonic noise and insufficient mechanical strength. In this work a new spherical TEPC was developed. The approach used was to divide the cathode in several rings with different thicknesses, and adjust the potential difference between each ring and the anode to produce an electric field that is nearly constant along the length of the anode. A-150 tissue equivalent plastic is used for the

detector walls, the insulator material between the cathode rings is low density polyethylene, and the gas inside the detector is propane. The detector, along with the charge sensitive preamplifier, is encased in a stainless steel vacuum chamber. The gas gain was found to be 497.5 at 782 volts and the response to neutrons as a function of angle was constant ±7%. This spherical tissue equivalent proportional counter detector system will improve the accuracy of dosimetry in space, and as a result improve radiation safety for astronauts.

To my two stars, Alfonso and Irene Deneb, my muses, and the loves of my life.

ACKNOWLEDGEMENTS

I wish to express my eternal gratitude to my advisor, Dr. Leslie Braby, for his guidance and encouragement during my research. He introduced me to this wonderful research field of space radiation, and gave me the opportunity of a life time.

I want to thank Dr. John Ford. Since the first day I landed at the TAMU Nuclear Engineering Department looking for a spot in the graduate program, he has trusted and supported me unconditionally; he has been a college and life mentor for me and my family. I also want to thank his wife, Dr. Virginia Ford, and their kids, Eli and Maggie because they have gone the extra mile for me and my family.

I also want to thank the members of my advisory committee: Dr. John Poston (who was my teacher during one semester), Dr. William S. Charlton, and Dr. Rainer Fink for their support, helpful comments and suggestions during the research.

My sincere gratitude to Dr. Mark Everett from TAMU Geology and Geophysics and Elaine Everett (my husband's advisor and his wife) for helping us during this journey and for their friendship.

Special thanks go to the Department of Physics Machine Shop staff for their help in the mold construction.

My gratitude to The Radiation & Space Biotechnologies Branch of NASA Ames Research Center, Crew Exploration Vehicle (CEV), Mission Services, Lockheed Martin, Health Physics Society, Roy Post Foundation, and TAMU Department of Nuclear Engineering for sponsoring part of my PhD studies.

Also, I want to thank Margit Garay and the International Student Services at Texas A&M University crew for helping me with all the necessary paperwork to “preserve” my non-resident alien immigration status.

I wish to thank friends and officemates during my stay: Dr. Leticia Espinosa, M.Sc. Temeka Taplin, Dr. Natela Ostrovskaya, Dr. Amy Malowsky, Dr. Alex Pasciak, and Susan Ondrasek for their support and companionship, they have made this journey very pleasant and enjoyable.

Also, I want to thank the Department of Nuclear Engineering and the Nuclear Science Center staff for their support, especially Alfred Hanna.

I want to thank Stephanie Morehead, Heather Heitpas, Lorie Burns, teacher assistants and staff at Texas A&M Becky Gates Children’s Center for giving me the peace of mind about my child care during this journey.

I want to thank my mom, Yolanda, because she has a direct phone line with God, and she used to ask Him for all my needs, for her unconditional love and support.

I want to thank my dad, Jesus Alberto, because he taught me I am capable to do whatever I dream about, and also for his love and advice.

Thanks to my family: Jesus Alberto Jr., Felix A., Estephanie, Silvia, Mireya, Marisol, Felix E., Luis, Jesus and Oscar Baloa, Ysabel, Jesus Antonio, Jesmir, Oscarcito, Natalia, Carolina, Grecia, Jonathan, Luisma, Reina, Yajaira y Estelita for being in my “fan’s club”; they have been cheering me up my whole life.

I want to thank my grandparents, Felix and Delia; they have been a lighthouse on my life, and even though they are not physically with us anymore, I will always keep their spirits and wisdom deep in my heart

I am grateful to my cousin Daniel, who was taken from us at a very young age. I feel I have to keep moving forward on his behalf because he did not have the chance.

And last but not least, to my husband, Dr. Alfonso Benavides Iglesias, for his support and patience during this long journey, for suggesting me how to improve my manuscripts, for translating from “my English” to “everybody else’s English”, and for

believing in me even during those times that I could not believe in myself. Also for 14 years of love, friendship and companionship.

TABLE OF CONTENTS

LIST OF FIGURES

FIGURE Page

FIGURE Page

LIST OF TABLES

CHAPTER I

INTRODUCTION

1.1. Space Dosimetry

Tissue-Equivalent (TE) proportional counters are used for biological and medical dosimetry whenever a mixture of high and low LET radiation is present. They are also being used for space radiation dosimetry. Space radiation consists primarily of directly ionizing radiation in the form of high-energy, charged particles. There are three naturally occurring sources of space radiation: trapped radiation, galactic cosmic radiation (GCR), and solar particle events (SPE).

It is thought that flow patterns of the Earth's molten iron and nickel outer core creates electric currents that give rise to the main geomagnetic field inside and around the Earth. The magnetic field extends several thousands kilometers out from the surface of the Earth. The trapped radiation or Van Allen belts are created primarily by particles produced by the Sun that become trapped in the Earth's magnetic field. The Van Allen radiation belts are doughnut-shaped zones surrounding The Earth, the inner Van Allen belt dips down to about 200 km into the upper region of the atmosphere over the South Atlantic because the center of the magnetic field is offset from the geographical center of

---

This dissertation follows the style of Health Physics.

the Earth by 448 km.The inner belt contains protons with energies exceeding 10 MeV. The outer belt contains mainly electrons with energies up to 10 MeV.

Galactic cosmic rays consist of ionized atomic nuclei originating outside the solar system and accelerated to very high energies, producing average dose rates of 10 μGy per hour in cislunar space and 6 μGy per hour on the lunar surface. Neutrons created by cosmic rays colliding with the spacecraft main body and external facilities are postulated to be a potential risk to astronauts (Kastner et al., 1969).

Cosmic rays essentially include all of the elements in the periodic table up to uranium; about 90% of the nuclei are hydrogen (protons), 9% helium nuclei, and about 1% heavier elements such as carbon, oxygen, magnesium, silicon and iron. Because cosmic rays are electrically charged they are deflected by magnetic fields, including the interplanetary magnetic field embedded in the solar wind (plasma of ions and electrons blowing away from the solar corona at about 400 km/sec), and therefore they have difficulty reaching the inner solar system. Spacecraft venturing outwards to the boundary of the solar system have found that the intensity of galactic cosmic rays increase with the distance from the Sun. The solar wind repels low energy galactic cosmic rays, decreasing the dose by a factor of two during solar maximums.

Solar Particle Events are ejections of energetic electrons, protons, helium nuclei, and heavier particles into interplanetary space. These particles are accelerated to near-

relativistic speeds by interplanetary shock waves which precede fast coronal mass ejections. Coronal mass ejections are closely related to active solar regions and appear in the vicinity of solar flare sites. The Sun's activity is characterized by an 11-year cycle in the occurrence of active regions. On average, it can be divided into four inactive years, and seven active years. From the prospective of active region magnetic polarity, the solar activity has a 22-years cycle, due to the fact that magnetic polarity in the north and south solar hemispheres reverses every 11 years.

As NASA makes plans to send manned spaceflight missions back to the Moon and Mars, radiation protection for crew members remains one of the key technological issues which must be resolved. NASA will require measuring the absorbed dose D, equivalent dose H, and also recording the energy spectrum in the crew exploration vehicles. The expected radiation environment will be high dose rate, mostly due to protons. For this type of radiation environment, microdosimetry will probably be used because it can give more information than conventional dosimetry.

1.2. Microdosimetry

Microdosimetric measurements are a powerful tool for characterizing mixed radiation fields like the one found in the space. One of the most important concepts in microdosimetry is the energy deposit, ε_i; namely, the energy deposited in a single interaction, i. Thus

$$\varepsilon_i=\varepsilon_{in}-\varepsilon_{out}+Q, \qquad 1.1$$

where ε_{in} is the energy of the incident ionizing particle, ε_{out} is the sum of the energies of all ionizing particles leaving the interaction, excluding rest energy in both cases, Q is the change in rest energies of the nucleus and of all particles involved in the interaction (ICRU Report 60, 1998). The energy imparted, ε, to the matter in a given volume is the sum of all energy deposits in the volume, defined as

$$\varepsilon=\sum\varepsilon_i. \qquad 1.2$$

ICRU also defines ε_s as the energy imparted to the matter in a given volume by a single event, but this quantity depends strongly on the size of the volume. A more convenient quantity is the lineal energy, y, thus

$$y = \frac{\varepsilon_s}{\bar{l}}, \qquad 1.3$$

where $\bar{l}$ is the mean chord length. Lineal energy is a random variable, and it is usually better to refer to the probability density of lineal energy, f(y). By definition, the probability density functions are normalized so that the area under the curve is 1.0,

$$\int f(y)dy = 1. \tag{1.4}$$

Another important quantity is the specific energy, z. This refers to all the energy deposited in the volume during the time of interest.

$$z = \frac{\varepsilon}{m}. \tag{1.5}$$

The units for z are the same as for absorbed dose, J/kg, with the same special name, Gray. Specific energy is also a random variable, and it is describe better a probability density function f(z), which is also normalized.

1.3. Current International Space Station Design

With the frequency and duration of space activities increasing, exposure to fast heavy ions from GCR is also of growing concern (Guetersloh et al., 2004). Astronauts are considered radiation industry workers considering the dose received during missions. From project Mercury until the first actual shuttle flight the doses received for the astronauts have been measured at between 0.23 mGy and 178 mSv per mission, as shown in Table 1.1. The doses on early missions were given in mGy because at that time it was not possible to measure the radiation quality factor Q. The risks to be considered for these doses are stochastic health effects. They include cancer, leukemia and genetic mutations. A major objective of space radiation research is to reduce the cancer risk for the astronauts.

Since Project Mercury, the doses received by astronauts have been a growing concern. The first Mercury missions did not have dosimeters because they were planned for altitudes that would not involve contact with the Van Allen radiation belts. Just before the MA-8 mission, manmade radiation was noted and personal dosimeters (thermo luminescent dosimeter, TLD) were added within the astronaut's suit and inside the spacecraft. The MA-8 and MA-9 flights revealed that the astronauts received doses less than 7 mSv.

Table 1.1. Doses receive for the astronauts (modified from SRAG, 2008).

Mission	Dose
Gemini 3	0.23 mGy
Gemini 4	0.46 mGy
Gemini 5	1.76 mGy
Gemini 7	1.64 mGy
Skylab	25 mGy
Apollo 11	1.73 mGy
Shuttle (Average Skin Dose)	~4.33 mSv/mission
Apollo 14 (Highest Skin Dose)	14 mSv/mission
Skylab 4 (Highest Skin Dose)	178 mSv/mission
Shuttle (Highest Skin Dose)	78.64 mSv/mission

Radiation exposure on Apollo missions was well documented. Each crew member had a personal radiation dosimeter, Figures 1.1 and 1.2, and three passive dosimeters, placed in the ankle, thigh and chest. Table 1.2 shows average radiation doses of the flight crews. They also had a radiation survey meter to determine radiation levels in any desired locations in their compartment in the event of a radiation emergency, Figure 1.3.

Table 1.2. Average radiation doses of the flight crews for the Apollo missions (modified from Bailey, 1975).

Apollo Mission	Skin Dose, mGy	Duration
7	1.6	10d 20h 09m 03s
8	1.6	06d 03h 00m 42s
9	2.0	10d 01h 00m 54s
10	4.8	08d 00h 03m 23s
11	1.8	08d 03h 18m 35s
12	5.8	10d 04h 36m 24s
13	2.4	05d 22h 54m 41s
14	11.4	09d 00h 01m 58s
15	3.0	12d 07h 11m 53s
16	5.1	11d 01h 51m 05s
17	5.5	12d 13h 51m 59s

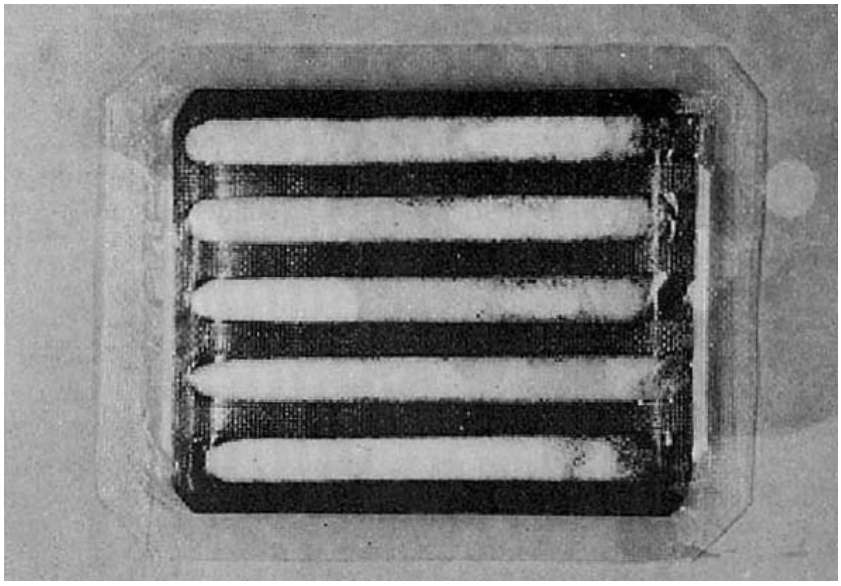

Figure 1.1. Passive dosimeter with component parts. Personal Dosimeters used during Apollo Missions. Reprinted with permission from Biomedical results of Apollo [online book], by Bailey V, 1975.

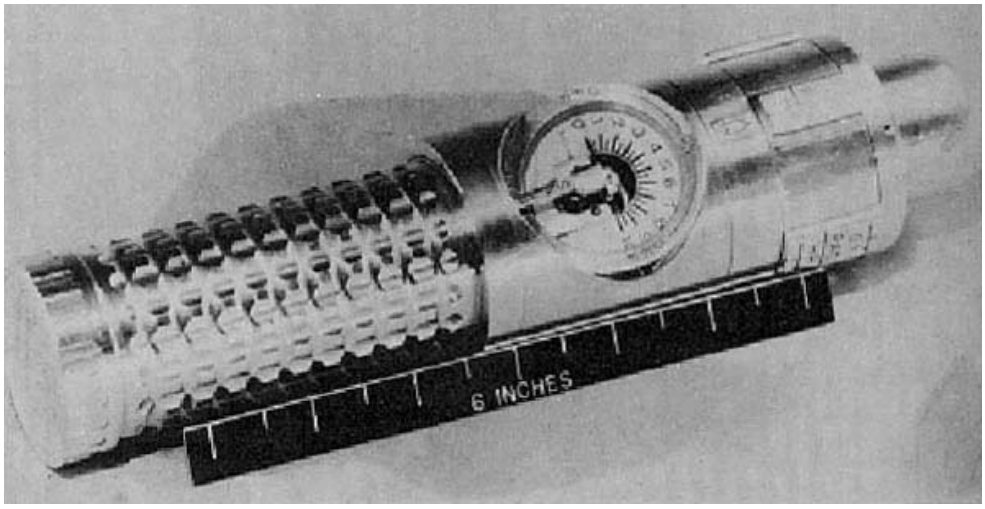

Figure 1.2. Radiation-survey meter. Radiation-survey meter used during Apollo Missions. Reprinted with permission from Biomedical results of Apollo [online book], by Bailey V, 1975.

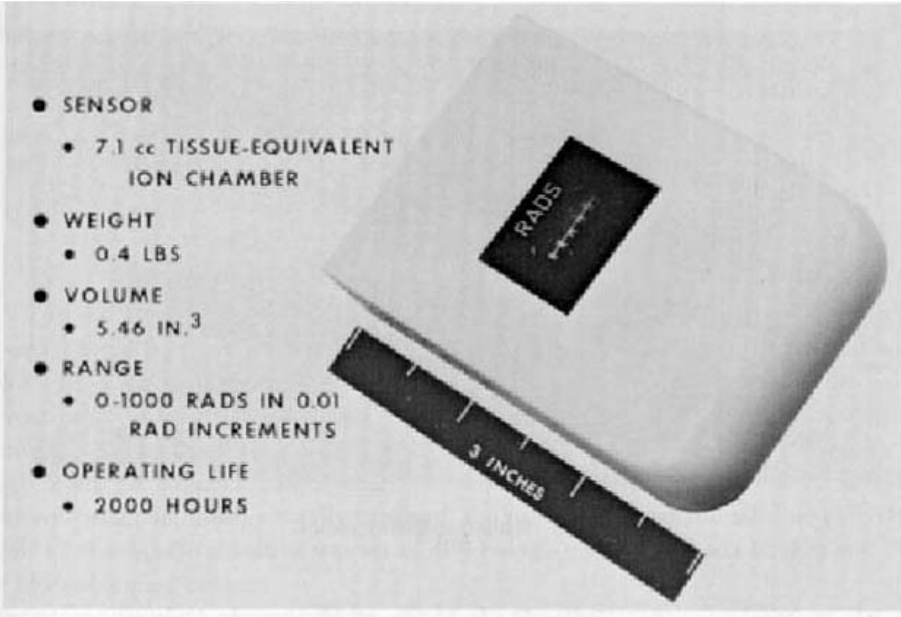

Figure 1.3. Personal radiation dosimeter. 7.1 cm^3 Tissue-Equivalent Ion Chamber used during Apollo Missions. Reprinted with permission from Biomedical results of Apollo [online book], by Bailey V, 1975.

Nowadays, dose on the space shuttles and the International Space Station (ISS) are monitored with the Radiation Area Monitor, a Crew Passive Dosimeter, Tissue Equivalent Proportional Counter (TEPC), and Charge Particle Directional Spectrometer, the latter is only found on the ISS.

International Space Station (ISS) generally has one TEPC on board; this is a cylindrical detector of 5.08 cm diameter by 5.08 cm long, filled with propane gas at 15 Torr to represent a 2 μm diameter volume of human tissue. The TEPC spectrometer has a dual multi-channel analyzer design with 1024 channels of low-gain data, and 256 channels of

high-gain data. This can operate with 120 V or 28 V power and use a RS-232 and 1553 communications ports, Figure 1.4.

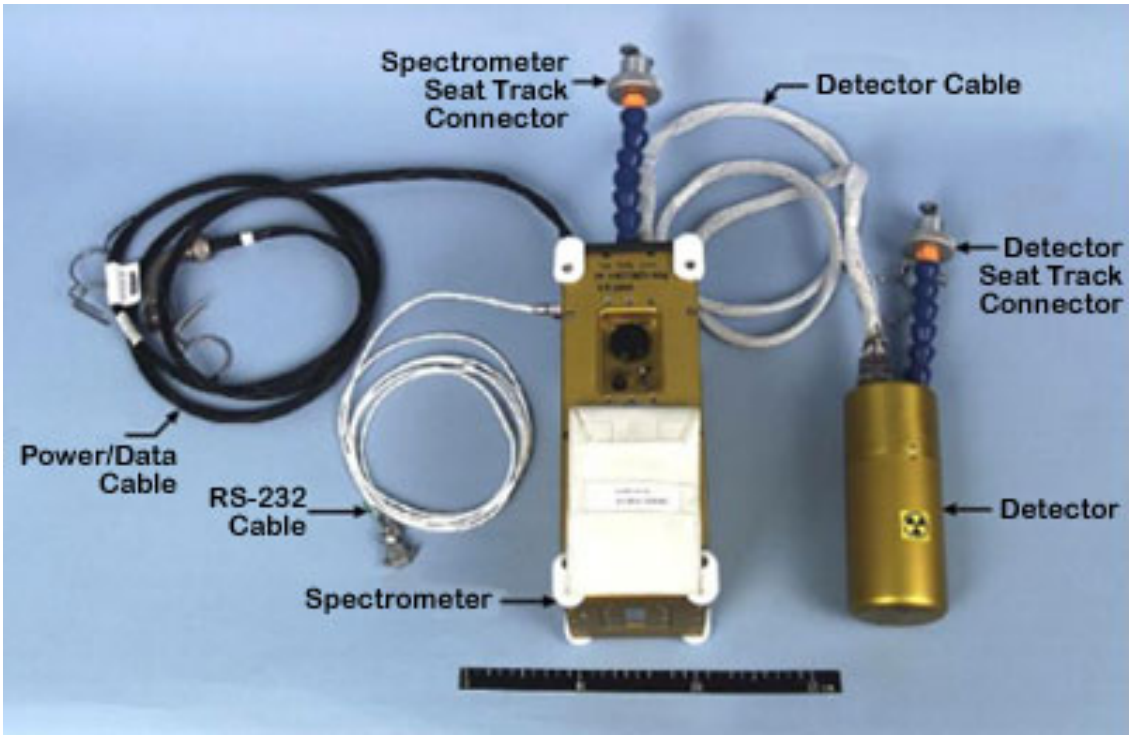

Figure 1.4. TEPC and spectrometer on board ISS and Shuttle. (SRAG, 2008)

There are several tissue equivalent proportional counter designs that have been developed for neutron dosimetry, but they are not appropriate for the high energies found in space. The preferred detector geometry is spherical in order to obtain an isotropic response, but simple spherical detectors have the disadvantage of non-uniform electric field along the detector's anode. In order to achieve a uniform electric field along the detector axis, spherical TE proportional counters have been designed with different structures to modify the electric field. Some detectors use a cylindrical coil that

is coaxial with the anode. There are also some commercially available spherical TE proportional counters that use the Benjamin design (Benjamin et al., 1968). A uniform electric field is achieved for part of the anode by placing disk electrodes at anode potential at the ends of the anode. This tends to compensate for the increase in field strength near the ends of the anode due to spherical shape of the cathode (Belonogii and Drobchenko, 1986).

The detector developed during this project makes use of a different approach for field correction; dividing the cathode into conductive rings, each of which is held at the required potential by a voltage divider.

The next chapter contains a detailed description of the calculations used to design the detector, and techniques used to build it. Chapter 3 describes the procedure to implement the detector for measuring the neutron dose rate, and the last chapter describes the results for detector angular response and lineal energy resolution.

CHAPTER II

SYSTEM DESIGN AND CONSTRUCTION

2.1. Objective

The objectives of the design studies were to:

- Design a 1.778 cm internal diameter spherical tissue-equivalent proportional counter using a segmented wall configuration to produce uniform gain along the length of the anode. This detector will be the prototype for the new dosimeters for the next generation of space vehicles.

- Determine the impact of wall thickness on neutron calibration using Monte Carlo simulations.

The prototype detector was built based on the results of these studies and limitations imposed by intended use in space.

2.2. Wall Thickness

The design of a TEPC to respond to indirectly ionizing radiation, such as neutrons, as well as charged particles, requires secondary particle equilibrium in the detector wall, or

an understanding of corrections needed if equilibrium is not possible. This requires data on the energy deposited in the cavity as a function of wall thickness. This data was obtained through Monte Carlo calculations of energy imparted by recoil particles in a fixed size gas volume surrounded by walls of different thickness and atomic composition. The accuracy of such estimates is limited by the accuracy of the available neutron cross section data and the methods for following recoil protons, but appears to be adequate for guiding the detector design.

In order to achieve ideal neutron dosimetry, it is important to determine an optimal wall thickness. The main consideration is to satisfy the secondary charge particle equilibrium (CPE) condition to make dose equal to kerma. The objective is for the dose in the wall to represent dose at a point in an infinite uniform medium like the human body. In order to comply with the CPE condition the wall thickness should be at least as thick as the range of a proton having the maximum energy of the neutrons to be monitored. However, thick walls will also attenuate low energy neutrons, resulting in an underestimate of their contribution to the total dose. Monte Carlo calculations were used to evaluate energy deposition per incident neutron in simulated low pressure propane-filled proportional counters as a function of the wall thickness.

2.2.1. Monte Carlo Simulation

MCNPX version 2.4.0 by Los Alamos National Laboratory was used for the simulations. The program was set up to calculate the track length estimate of energy deposition in a 0.9 cm radius sphere filled with propane with density of 2.59 x 10^{-5} g/cm^3, corresponding to a pressure of 10 torr (see equation 2.4, section 2.4), and resulting in a simulated site diameter of 0.47 μm in unit density tissue (see equation 2.3, section 2.4). The simulations were conducted for a monoenergetic and monodirectional 12 cm diameter plane disk neutron source located 50 cm away from the center of the propane sphere. Current information on neutron production processes suggest that there are probably two broad peaks in the neutron spectrum produced by galactic cosmic ray interactions with a spacecraft, around 10 and 100 MeV. Three groups of simulations were run for each of these two neutron energies.

Wall thicknesses of 0.5 cm, 1.0 cm, and from 1.5 cm to 8.5 cm on 1 cm intervals were used for the simulations. This range of thickness values was chosen because of the fact that the range of 100 MeV protons is about 7.57 g/cm^2 (Turner, 1995; p.130). An additional wall thickness of 0.1 cm was tested for 10 MeV neutrons because their maximum recoil proton range is 0.118 g/cm^2 (Turner, 1995; p.130).

No simulations for wall thickness below 0.1 cm were performed because building such thin shells requires a more elaborated fabrication technique and there is no guarantee

such a sensor can withstand real-scenario mechanic stresses. The material composition for the simulations is described in Table 2.1 for tissue equivalent plastic A-150, and in table 2.2 for stainless steel 303.

Table 2.1. Percent elemental composition, by weight, of A-150. Tissue-Equivalent Plastic Compared to ICRU Muscle Tissue (AAPM, 1980).

Element	**ICRU Muscle [a]**	**A-150 Plastic [b]**
H	10.2	10.2
C	12.3	76.8
O	72.9	5.9
N	3.5	3.6
Ca	0.007	1.8
F	not listed	1.7
Total	98.907	100

[a)] ICRU (1964); [b)] J.B. Smathers et. al. (1977)

The first group of Monte Carlo simulations was run using a tissue equivalent plastic spherical shell, filled with propane, with wall thicknesses described above, surrounded by air at standard conditions. This simulates the ideal cavity detector.

Table 2.2. Percent elemental composition, by weight, of Stainless Steel 303 (Sandmeyer Steel Company, 2008).

Element	Percent
Ni	9
Cr	18
Fe	69.81
Si	1
Mn	2
C	0.12
P	0.04
S	0.03

The second group uses the previous tissue equivalent spherical shell encased in a cylindrical stainless steel vacuum chamber 20.4 cm in diameter by 23 cm long with 0.16 cm wall thickness, filled with propane gas at the same density as the internal sphere. The diagram in Figure 2.1 shows two red circles that represent the maximum and minimum wall thickness. This simulates a simple, practical detector, useful in laboratory experiments.

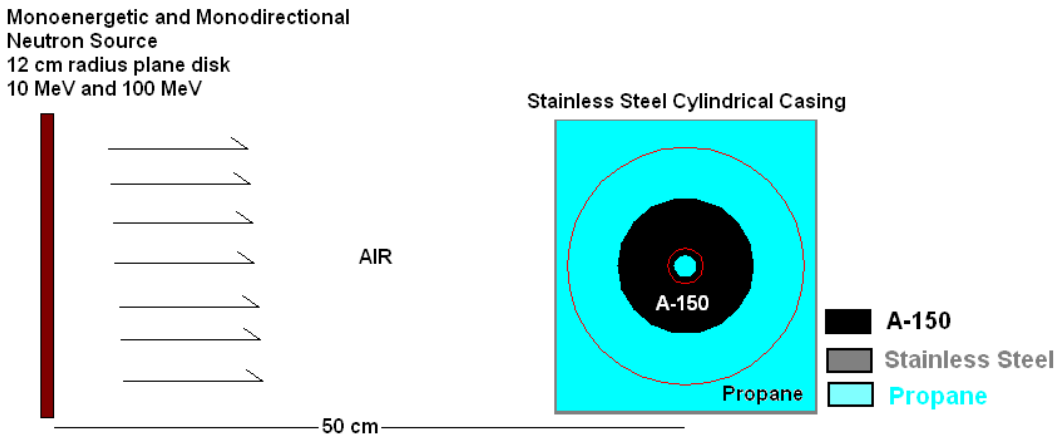

Figure 2.1. Constant vacuum chamber configuration. A-150 spherical shell in a cylindrical stainless steel vacuum chamber filled with propane gas at the same density as the internal sphere.

The third group has the same model elements as the second group of simulations but now the cylinder dimensions were modified accordingly to the size of the tissue equivalent spherical shell, so the space between the outer spherical and the inner cylindrical surfaces were kept constant; 1 cm in the radial direction and 6 cm in height. Extra space along the cylinder axis is intended for the preamplifier electronics, see Figure 2.2. This simulates a custom, compact detector which might be used on spacecraft.

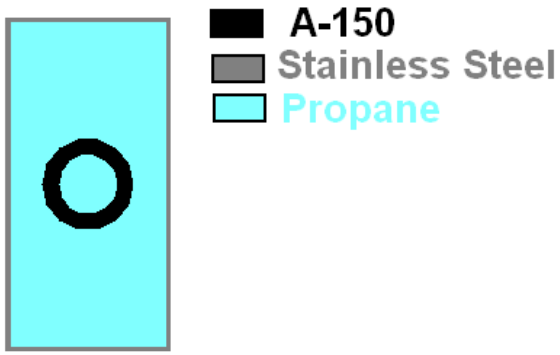

Figure 2.2. Proportional vacuum chamber configuration. A-150 spherical shell in a proportional cylindrical stainless steel vacuum chamber filled with propane gas at the same density as the internal sphere.

Finally, four additional simulations were run with a tissue equivalent buildup cap outside the stainless steel vacuum chamber since this is a common approach used in experimental dosimetry. To precisely measure the total dose in a mixed radiation field, some additional information can be obtained by making measurements with detectors with two different wall thicknesses. The difference between the readings of the thick and thin walled detectors will provide some information for estimating the error due to lack of secondary particle equilibrium in both detectors. The thick walled detector is often achieved by adding a buildup cap to the thin walled detector and making a second measurement.

The tissue equivalent shell wall thickness was 0.5 cm, the stainless steel cylinder dimensions were 2.4 cm radius by 10 cm height. Tissue equivalent buildup cap wall thicknesses were 0.5 cm and 1cm, as shown figure 2.3. The results of calculations for

energy deposition with a tissue equivalent buildup cap outside the stainless steel vacuum chamber will be compared with those for the same total wall thickness, entirely inside the vacuum chamber.

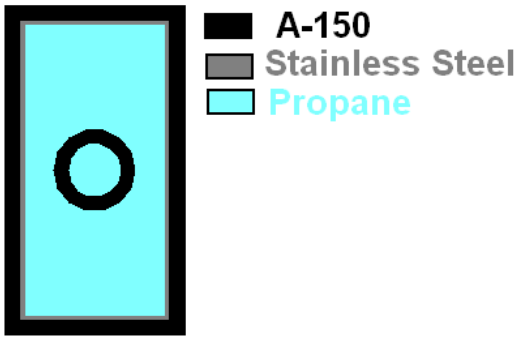

Figure 2.3. Buildup cap wall configuration. A-150 spherical shell in a proportional cylindrical stainless steel vacuum chamber filled with propane gas at the same density as the internal sphere.

The MCNPX surface cards are a set of text descriptors that define the geometry, atomic classes and abundances of the model, type of the particles involved and the geometry of the primary particle source, as shown Figure 2.4.

The cell cards descriptors include material number, material density (in this particular case in units of g/cm^3), and the geometrical space defined by the surface cards. The descriptor *mode* defines the particles followed in the simulation, *imp* is the importance of each particle in each different cell, *sdef* is the specification about type, position, and energy of the source, *nps* is the number of particular in the simulation. F6 indicates the tally to be used, the particles to be considered and the cell number where the tally is

calculated. The material cards show the elemental composition in each material to be used.

```
c det
c cell cards
1   2 -0.0000259 -1             $Inside sphere propane
2   3 -1.127 1 -2               $shere shell A-150
3   2 -0.00000216 -3 -4 5 2      $inside cylinder propane
4   4 -8.03 (3:4:-5) -6 -7 8    $cylinder walls steel
5   1 -0.00191 (6:7:-8) -9      $air
6   0 9

c surface cards
1   SO 0.889        $Internal Sphere
2   SO 1.389        $External Sphere
3   CY 10.2225       $Internal Cylinder
4   PY 11.4925
5   PY -11.4925
6   CY 10.38125      $Internal Cylinder
7   PY 11.65125
8   PY -11.65125
9   SO 100
10  PZ -50

mode n h
IMP:n,h 12 8 4 4 4 0
c Source specification cards
SDEF SUR=10 POS=0 0 -50 RAD=D1 DIR=1 erg=100 par=1
SI1 12
nps 1000000000
F6:n,h 1
c Material Specification
M1 006000 -0.02 008016 -0.28 007014 -0.70                      $air
M2 001001 -0.7273 006000 -0.2727                        $Propane C3H8
M3 001001 -0.102 006000 -0.768 008016 -0.0592 007014 -0.036 020000 -
0.018 009019 -0.017                                          $A-150
M4 028000 -0.09 024000 -0.18 026000 -0.6981 014000 -0.01 012000 -0.02
006000 -0.0012 015031 -0.0004 016000 -0.0003          $steel
```

Figure 2.4 MCNPX simulation example with vacuum chamber. A-150 spherical shell in a cylindrical stainless steel vacuum chamber filled with propane gas at the same density as the internal sphere

2.2.2. Effect of Wall Thickness

A billion particles were run in each simulation; the statistical errors produced by the simulation were between 0.9% and 6% for the 100 MeV simulations, and between 0.04% and 0.05% for 10 MeV simulations. Figure 2.5 shows that the track length estimate of energy deposition per neutron for 100 MeV neutrons increases as the wall thickness is incremented for the three groups of simulations, reaching a plateau when the wall thickness is approximating to the range of 100 MeV protons.

The simulations without the vacuum chamber show the lowest energy deposition, the other two groups of simulations depict very similar results. The difference between the simulations run with the sphere without and with the vacuum chamber may be attributed to low energy neutrons reaching the spherical tissue equivalent shell. There was no notable difference between the constant and the proportional stainless steel vacuum chamber simulations. Only for 0.5 cm, 1 cm and 1.5 cm wall thickness was the difference more than 2%. A 0.5 cm wall thickness shell with a 0.5 cm and with a 1 cm wall thickness buildup cap is equivalent to the 1 cm and 1.5 cm wall thickness entirely inside the vacuum chamber respectively, with any differences less than the 3% statistical error.

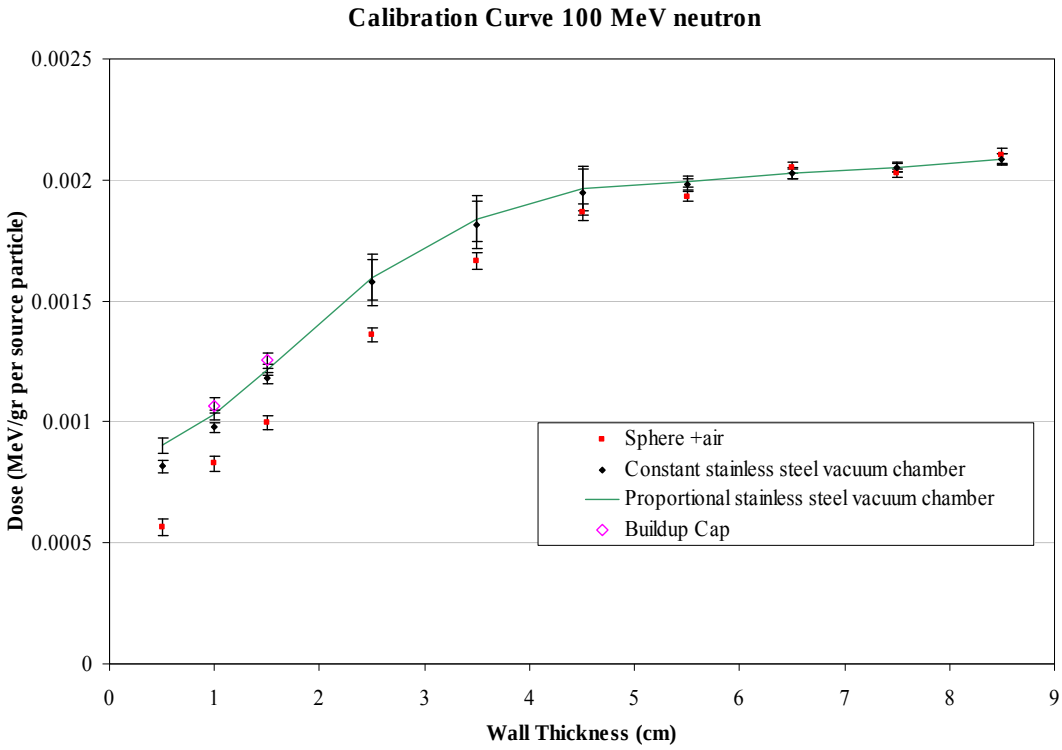

Figure 2.5. Calibration Curve for 100 MeV neutrons.

The relative error was defined as:

$$\text{relative error} = \frac{D_{CPE} - D_w}{D_{CPE}} \cdot 100\% \quad , \qquad 2.1$$

where D_{CPE} is the dose calculated for the charge particle equilibrium wall thickness. The relative dose error observed for the 0.5 cm walled detector (without secondary particle equilibrium) was 57% for the configuration with the proportional vacuum chamber, 61%

for the configuration with the constant vacuum chamber, and 73% for the configuration without vacuum chamber.

The buildup cap simulations show behavior similar to that in the 100 MeV case. The energy depositions for the buildup cap simulations are 3% more than those for the same wall thickness, entirely inside the vacuum chamber.

Figure 2.6 shows that the track length estimate of energy deposition for 10 MeV neutrons decreases as the wall thickness is incremented for the three groups of simulation. In contraposition with the 100 MeV simulations, the configuration without the vacuum chamber show the highest energy deposition, the other two groups of simulation depict very similar results. The relative dose error observed, in the 10 MeV case, for an 8.5 cm wall thickness detector was around 25% for all three configurations.

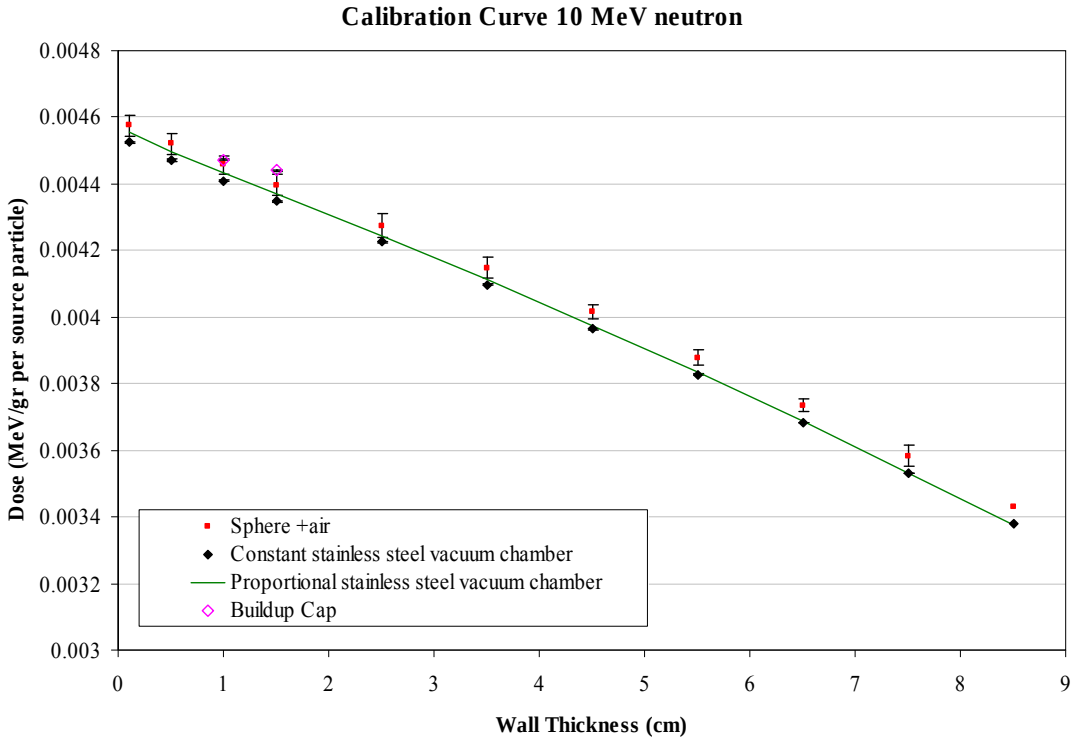

Figure 2.6. Calibration curve for 10 MeV neutrons.

The results for 100 MeV show that if the walls are not thick enough to produce charge particle equilibrium the dose is underestimated because there are fewer charged particles depositing energy in the detector site than there would have been if CPE existed. Also for a wall thicker than the maximum 100 MeV protons range, 7.57 g/cm^2, the energy deposited in the volume is lower because the incident neutrons are attenuated in the wall, and again the result is an underestimation in the dose.

The difference in energy deposition for the configuration with and without the vacuum chamber may be related to the low energy neutron attenuation or buildup of low energy neutrons produce be scattering in the stainless steel. For thinner walls, the dose will be lower for the “without chamber” configuration. This difference can be decreased by increasing wall thickness. After the wall thickness reaches the CPE the difference is inside the error bars.

The maximum dose is observed at 0.1 cm wall thickness for the 10 MeV simulations. The energy deposited decreases after that because incident neutrons are attenuated in the wall. Again the difference in energy deposition for the configuration with and without the vacuum chamber may be related to the low energy neutron attenuation or buildup of low energy neutrons produce be scattering in the stainless steel. This difference will decrease as the wall thickness is increased, but for all cases the error was under 2%.

Simulations run with the buildup cap showed a higher energy deposition than the models with the tissue equivalent entirely inside the vacuum chamber analog. This may be attributed to the simulation geometry; the neutron source is simulated as a monoenergetic and monodirectional plane source, and some neutrons are scattering into the detector from the buildup material outside the external diameter of the thick walled detector. If the TEPC is exposed to an isotropic neutron source, the energy deposition may be the same in both cases.

2.2.3. Compromise with Size and Weight

Unfortunately, it is not possible to use a wall thickness that provides an ideal response for neutrons of all energies in the range of interest since a wall that is thick enough to provide secondary particle equilibrium for high energy neutrons will attenuate the low energy neutrons in the spectrum. Choosing a TEPC with 0.5 cm wall thickness, which will underestimated 100 MeV neutron dose by 57%, may be acceptable where size and weight of the detector are important considerations; this wall thickness results in 1% attenuation for 10 MeV neutrons.

Even though it is extremely difficult to provide a precise measurement of the total dose produced by mixed radiation field, some additional information can be obtained by making measurements with detectors with two different wall thicknesses. The difference between the readings of the thick walled and thin walled detectors will provide some information for estimating the error due to lack of secondary particle equilibrium in both detectors. In a practical instrument, assuming that the radiation field is constant for long enough to make two dose measurements, the thick walled detector can be achieved by adding a buildup cap to the thin walled detector and making a second measurement.

2.3. Laminated Design

There are many considerations to take into account in the design of proportional counters; one of them is the detector geometry. Spherical detectors are preferred for many applications because of its relatively simple chord length distribution and isotropic response.

The main challenge in designing a spherical detector is to create a uniform electric field along the axis of the detector. Because the distance between the spherical shell and the anode wire placed along the diameter of the sphere is not constant, the electric field will be stronger and the gas gain will be higher near the ends of the anode. There are several techniques that can be used to correct this problem. The approach to be used here is to divide the cathode (spherical shell) into several rings with different thicknesses, and adjust the potential difference between each ring and the anode to produce an electric field that it is nearly constant along the length of the anode. This choice in design has an important advantage over using a grid around the anode because it produces considerably less microphonic noise.

The material used for the detector walls is a tissue equivalent (TE) conductive plastic A-150 (developed at the Physical Sciences Laboratory, Illinois Benedictine College, Lisle, IL, and currently manufactured by Exradin, a division of Standard Imaging). It has been widely used for constructing ionization chambers, biological and medical neutron

absorbers, and as the radiation energy absorber in instruments for calorimetric neutron dosimetry. A-150 is 45.14% polyethylene, 35.22% polyamide (du Pont nylon Zytel® 69), 16.06% carbon black, and 3.58% calcium fluoride by weight and its density is 1.127 g/cm^3 (Goodman, 1978). The insulator material between the cathode rings is a low density polyethylene. The gas inside the detector is propane, C_3H_8, at a pressure of 47 torr to simulate a 2 μm site size. TE sphere is encased in a 303 stainless steel cylinder 6.5 cm in diameter by 9.1 cm long.

2.3.1. Calculation of Segments

The calculation to estimate the thickness of each ring was made using an electrostatic model for an infinite cylindrical capacitor. The potential difference between the anode wire and some other cylinder with radius r_x inside this capacitor is given by

$$V_1 - V_x = (V_1 - V_2)\frac{\ln\frac{r_x}{r_1}}{\ln\frac{r_2}{r_1}} \qquad 2.2$$

Equation 2.2 corresponds to two concentric infinite cylinders with radius r_1 for the internal cylinder (anode) and r_2 external cylinder (sphere shell internal radius) at V_1 and V_2 potentials respectively. The electric potential differences between successive rings and the anode were chosen to be 100%, 95%, 90%, 85%, and 80% of the maximum

applied voltage. Assuming a sphere internal diameter of 1.778 cm and an anode of 0.00254 cm, this result in ring middle diameters of 1.778, 1.281, 0.923, 0.666 cm, as shown in Figure 2.7. To achieve these radii at the center of the rings and produce a spherical cavity the ring thicknesses are 0.470, 0.233, 0.095, 0.045 and a top of 0.523 centimeters (from the equator to the pole).

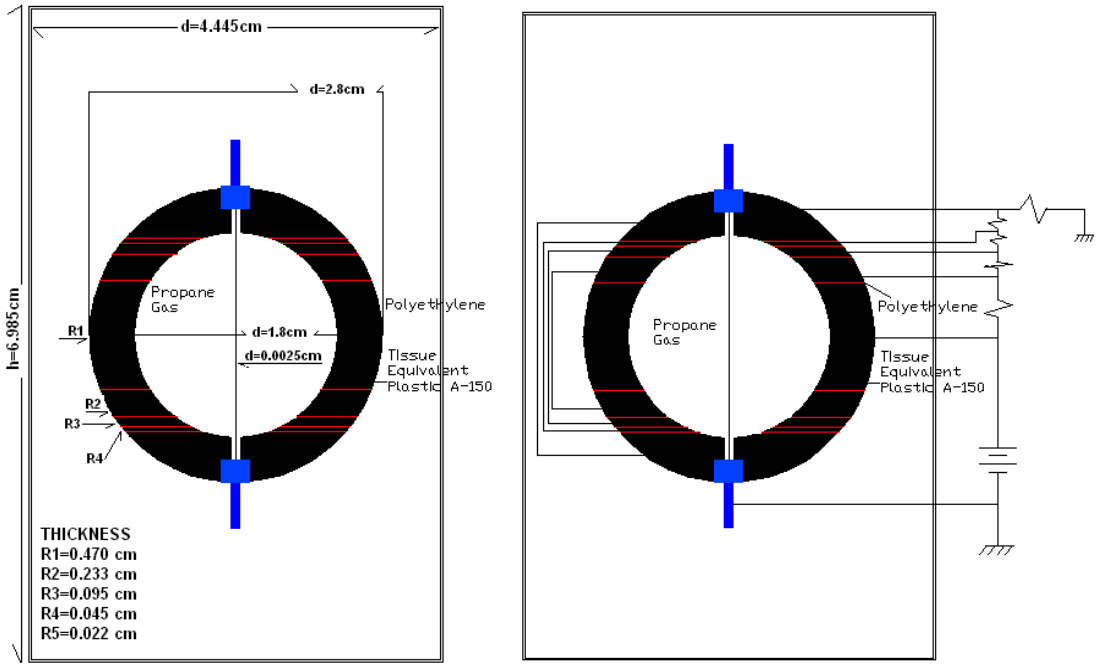

Figure 2.7. Detector cross-section. Left: parts dimensions and materials. Right: Electrical connections for the disks and anode wire.

2.3.2. Construction of Hemisphere

The procedure for building the spherical wall requires assembly of two hemispheres each consisting of four rings and a top piece. The TE plastic rings are fused to polyethylene insulating layers. The inner and outer surfaces of each ring follow the spherical profile. Each ring was molded individually, and then the stack was fused together to make the hemisphere.

The mold for making the rings and assembling them into hemispheres consists of three parts. The first part, the ends of the mold, consists of two solid brass disks one with a hemispherical central protuberance corresponding to the internal diameter of the shell, and the other with two stainless steel rods for aligning the disks which make up the outer wall of the mold. These disks are shown in the top of Figure 2.8.

The other two mold parts are two sets of brass disks, all with the same outside diameter and holes for the alignment rods. For each set the disk's thicknesses were cut to the desired thickness of the hemispherical shell segments. They were then stacked together, interspaced with 0.005 inch brass sheet, and a hemispherical cavity was machined in each set. One set with the sphere external diameter, as shown in the bottom-right of Figure 2.8, and the other with the internal diameter as shown in the bottom-left of Figure 2.8. Each disk in the external set has a groove to accommodate a 20 gauge wire entering the cavity.

Each plastic disk was molded separately by substituting the specific disk from the sphere external diameter brass disk set (4 in Figure 2.8) into the sphere internal diameter brass disk set. The solid brass disk (2) and the internal diameter brass disk set (3) (with the disk substitution), assembled on the base (1), were heated inside a laboratory oven at 155^{o}C (Braby and Johnson, 1995). A piece of 20 gauge stainless steel aircraft wire was placed in the grove of the external diameter disk to provide the appropriate electric connection to the plastic.

Figure 2.8. Mold parts. Top: disk with two stainless steel rods and solid brass disk with a central protuberance. Bottom: two cylindrical sets of brass disks.

After 4 hours the required amount of A-150 plastic, based on the weight of the ring plus 5%, was poured into the mold. After the plastic was heated for 45 min at 155^{o}C, the

mold was closed and compressed using a hydraulic press. After cooling the mold was disassembled, leaving the TE plastic disk inside its respective brass disk. Polyethylene layers were cut using the corresponding 0.005 inch brass sheet from the internal diameter disk set as a template. The set of plastic/brass disks corresponding to a hemisphere were stacked with the polyethylene layers between them to provide electrical isolation, as depicted in Figure 2.9. The whole stack of layers is then heat-bonded in a laboratory oven at 155^{o}C for 45 min, and slightly compressed with a hydraulic press. The same procedure is repeated for building a second hemisphere. Each hemisphere is tested with a high voltage ohm-meter to verify there is the appropriate electrical isolation between adjacent disks.

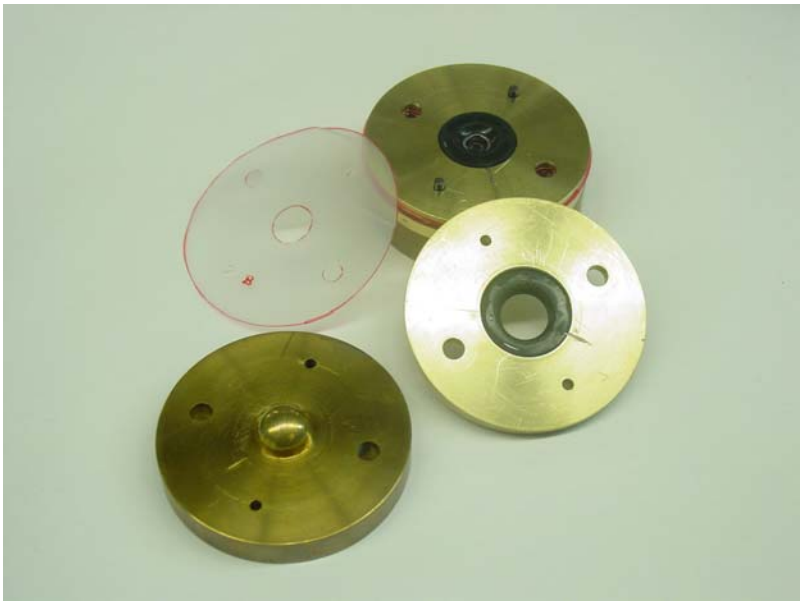

Figure 2.9. Preassembled hemisphere. The whole set of plastic/brass disks corresponding to a hemisphere will be stacked, lying polyethylene layers between them to provide electrical isolation.

Finally, the sphere is assembled. To assure proper alignment of the hemispheres three equidistant holes were machined in the mating surface of each hemisphere. On one of the hemispheres, three polyethylene screws are inserted, leaving about 1mm outside for connecting into the other hemisphere. The whole spherical sensor is held together by a clamp consisting of two circuit boards held together by 4 screws, making it easy to open when a new anode wire needs to be installed.

2.4. Detector Assembly

The sensor was assembled after machining the anode feedthrough holes. The anode is a stainless steel 304 hard temper wire 0.00254 cm in diameter (manufactured by California Fine Wire Company). The anode is isolated from the cathode using 30 and 24 gauge TFE (polytetrafluoroethylene, more commonly known as Teflon) tubes and Kel-F® bushings (PolyChloroTriFluoroEthylene is a fluorocarbon-based polymer and is commonly abbreviated PCTFE. The Kel-F® brand is a registered trademark of 3M).

An additional cylindrical cavity, concentric with the hole for the anode, was drilled in each pole to support the sphere with a Kel-F bushing. The bushing is glued to the first preamplifier stage board on one side and to a voltage divider board on the other side. The 30 gauge tube goes from the boards, passing through the sphere pole holes to the sphere inner surface The Kel-F bushing and 24 gauge tube run through the circuit boards and ends in a cavity machined in the sphere wall as shown figure 2.10.

The anode is at ground potential. On the preamplifier board, the anode is attached to a spring (piano wire) supported by a ceramic standoff that serves as a 0.4 pF feedback capacitor. From the ceramic standoff/feedback capacitor, there is a wire connected to the NJFET gate of the preamplifier, as shown in the left side of Figure 2.11.

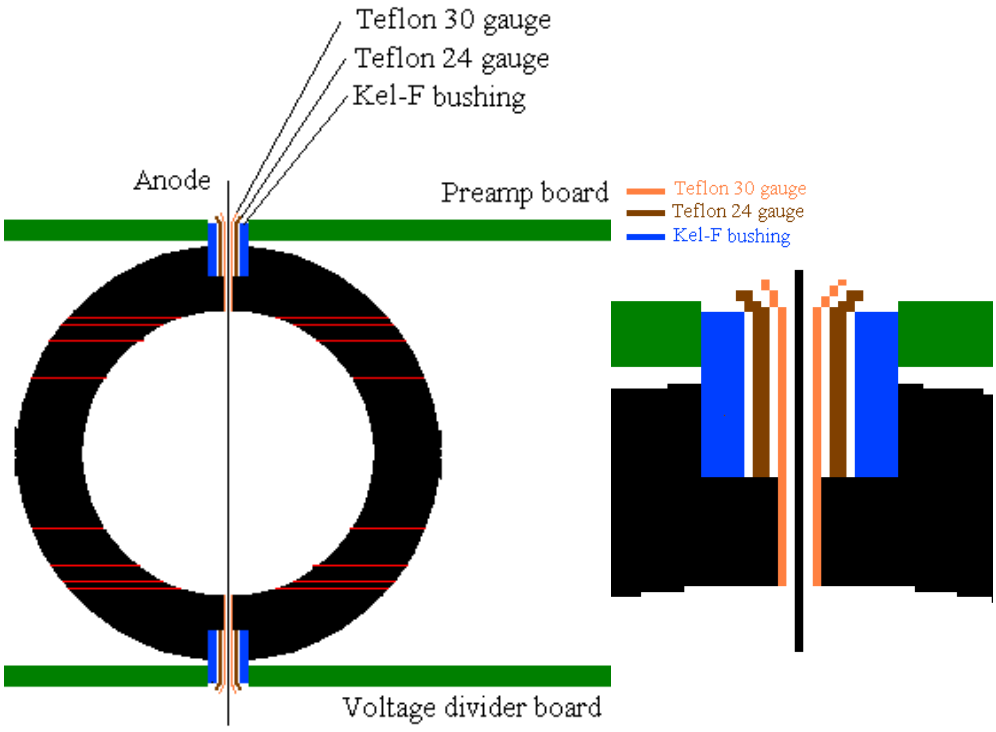

Figure 2.10. Boards and detector assembling. Left: detector between voltage divider and preamp. Right: enlarged view showing the Kel-F and TFE tubing to isolate the anode wire from the top shell conductor.

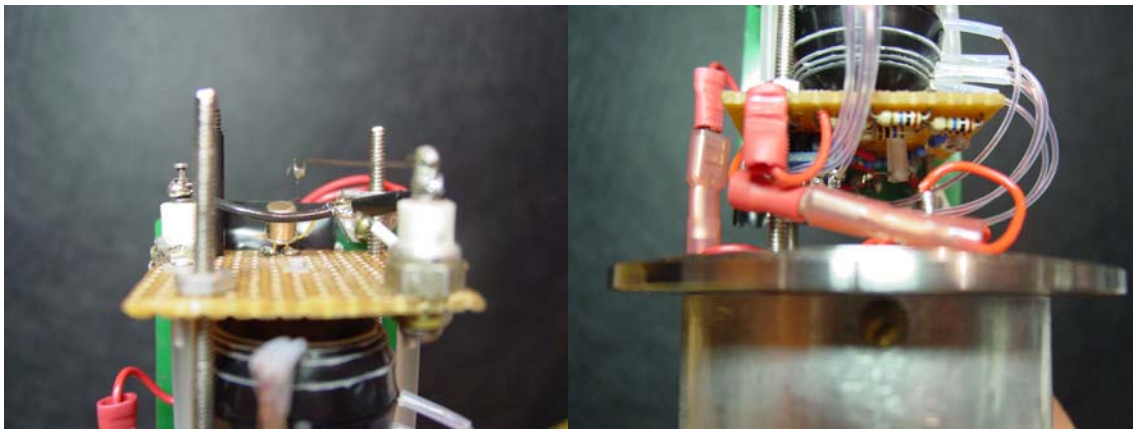

Figure 2.11. Top and bottom sensor boards. Left: first preamplifier stage board; Right: voltage divider board.

The NJFET gate with the anode wire is not routed using the preamplifier board because the board material has a significant dielectric constant and noise would be easily induced through the anode. A Kel-F standoff supports the anode wire at the voltage divider board, as shown in the right side of Figure 2.11.

Two Kel-F posts are used to keep the whole configuration together. The tissue equivalent proportional counter, preamplifier and voltage divider boards, as depicted in Figure 2.12, are encased in a 9.1 cm long by 6.5 cm diameter cylindrical 303 stainless steel vacuum chamber filled with propane at 47 torr.

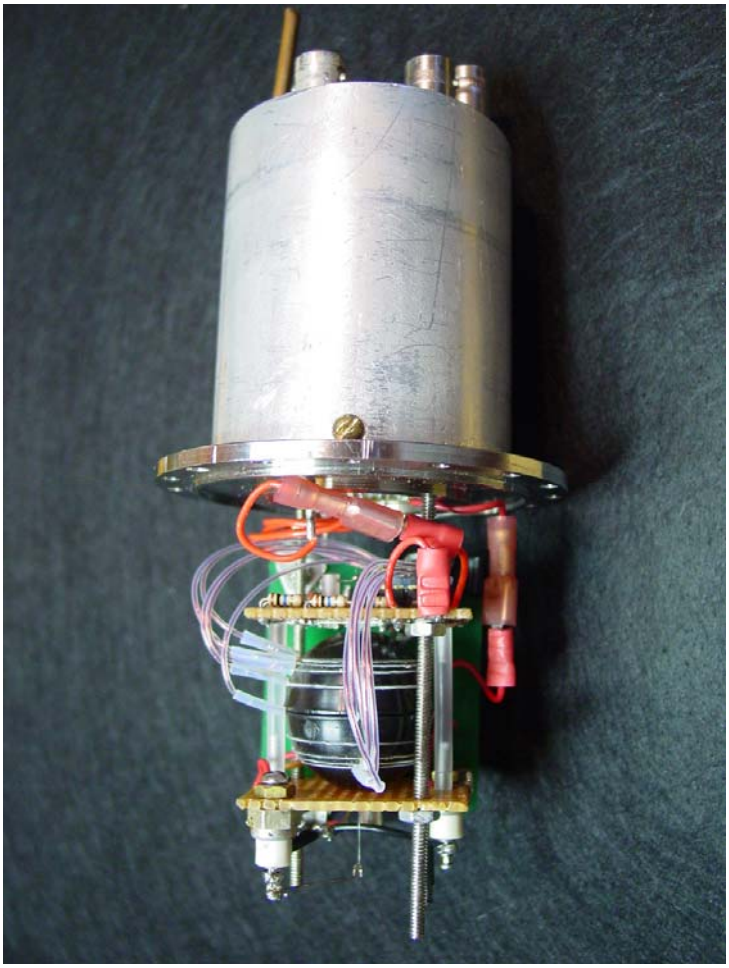

Figure 2.12. Tissue equivalent proportional counter. TEPC with preamplifier and voltage divider.

This gas pressure was determined by specifying that the detector would simulate 2 μm diameter tissue site. The gas filled cavity diameter is 1.778 x 10^{-2} m, and the tissue density is 1 g/cm^{-3}. The gas density is given by

$$\rho_T d_T = \rho_g d_g \,. \qquad 2.3$$

Substituting the values, the desired gas density is 9.48 x 10^{-5} g/cm^{-3}. Using the Ideal Gas Law

$$PV = \frac{m}{M}RT \quad , \tag{2.4}$$

where ρ=m/V, M is propane molar mass (44.096 g/mole), R is ideal gas constant (8.21 x $10^{-5}m^{-3}$atm $mole^{-1}$ $^{o}K^{-1}$) and T is the temperature (298.15 ^{o}K). The required gas pressure is 47 torr.

The vacuum chamber was sealed using 0.050 diameter Indium wire gasket (manufactured by Electronic Space Products International). The detector was initially degassed with a rotary vane vacuum pump down to a gas pressure about 10^{-2} torr, followed by a turbomolecular vacuum pump to reach a final gas pressure of 10^{-6} torr as depicted in Figure 2.13. During the whole degassing process the detector was in a hot plate at 100^{o}F. Preliminary tests were made after six hours of degassing in the vacuum system. After several more days at vacuum to remove absorbed gasses the detector was filled with propane and the detector's copper tube vacuum connection was sealed using a hand operated pinch off tool. Torr Seal® (Varian), a two part epoxy designed for vacuum applications, was used to cover the copper seal and protect it from mechanic damage.

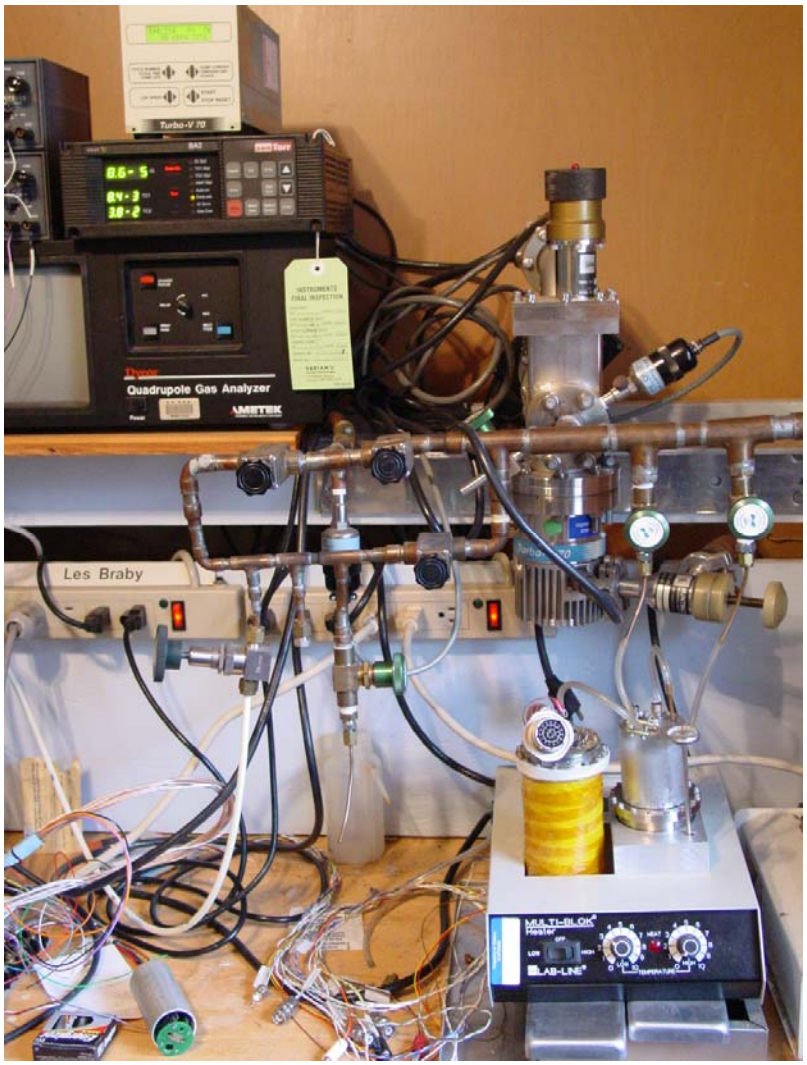

Figure 2.13. Detector in the vacuum system. The hot plate with the detector inside can be seen at the bottom right corner. Each detector is connected to the vacuum valves with polyvinylchloride (PVC) tube, the turbo pump and the senTorr is shown at the top.

2.5. Electronics

The detector anode is connected to a NJFET gate that is the input to a charge sensitive, low noise preamplifier shown in Figure 2.14 designed for Rossi proportional counters by V. Radeka (personal communication). The preamplifier provides 2.5 x 10^{12} V/coulomb charge conversion and a low impedance output to couple to a standard spectroscopy amplifier.

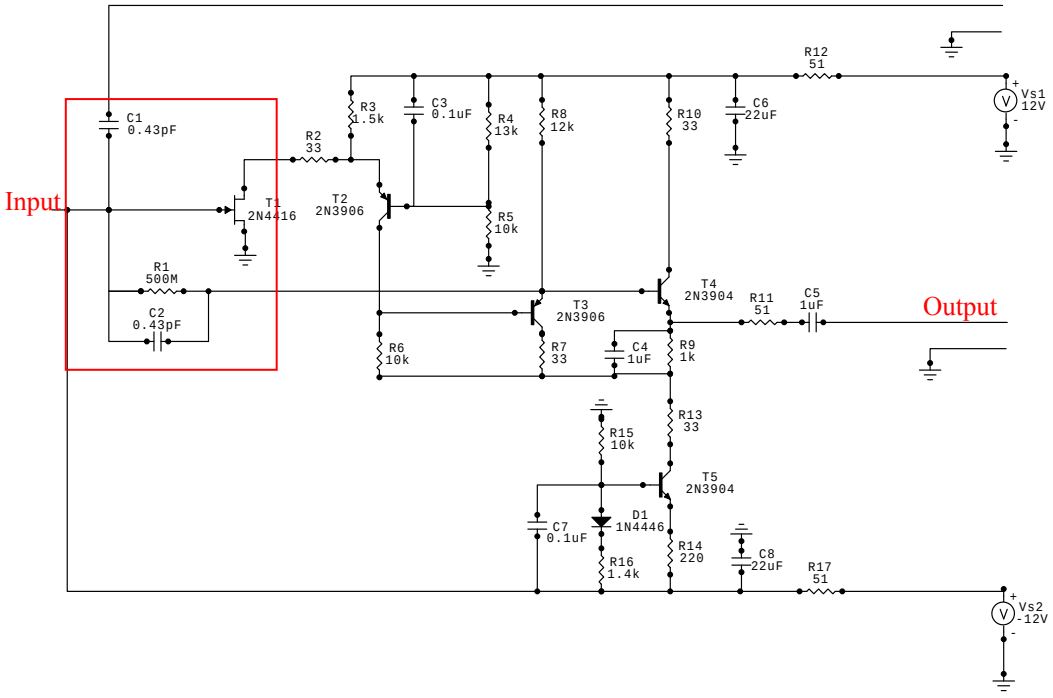

Figure 2.14. Low noise preamplifier for Rossi proportional counters by Radeka. The red square denotes the preamplifier first stage. Left: preamplifier input; right: preamplifier output. C1 and C2 are the two ceramic posts. The right top and bottom corners show the voltage supplies for the preamplifier.

Initially, TEPC detectors were built with the preamplifier outside the vacuum chamber; most recently, the first preamplifier stage was placed inside the vacuum chamber. This detector has the entire preamplifier inside the vacuum chamber to reduce any stray capacitance. Stray capacitance is an unwanted effect that can allow noise signals to leak into the circuit. A long wire between the anode and the NJFET can produce this unwanted noise. Figure 2.15 shows a block diagram of the whole electronic system, the shaded box shows the components inside the vacuum chamber.

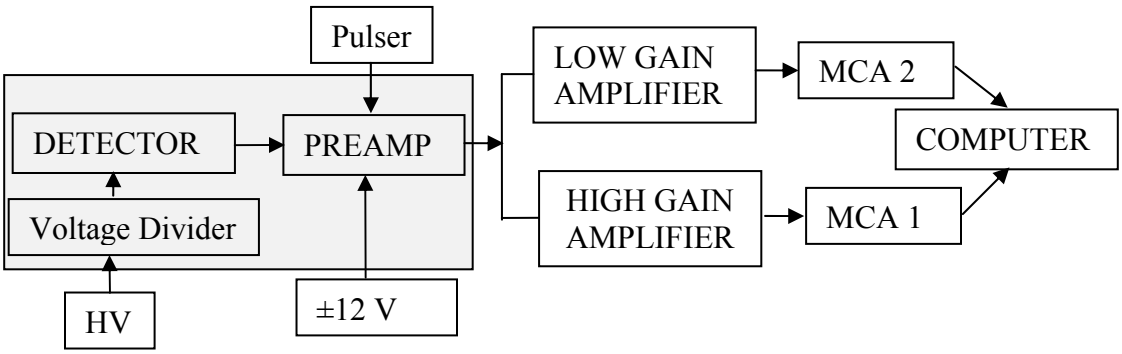

Figure 2.15. Block diagram. Basic diagram of the electronic system.

The voltage supply for the preamplifier is an Ortec Power Supply model 402M, the test pulser is an Ortec Pulser model 480, and the high voltage power supply is an Ortec Detector Bias Supply model 428, as shown in Figure 2.16.

The high voltage is connected to a RC filter to reduce the signal noise. The filter is connected to the voltage divider placed inside the vacuum chamber. Figure 2.17 shows the voltage divider in the shaded square, located inside the vacuum chamber, and the

high voltage filter located at the top outside of the vacuum chamber. Several resistors were connected in series in order to meet the voltage requirements. Due to this configuration the voltage applied to the detector is 92% of the supply voltage.

Figure 2.16. Detector's NIM bins. Left: Power Supply and amplifiers. Right: detector Bias Supply and Pulser.

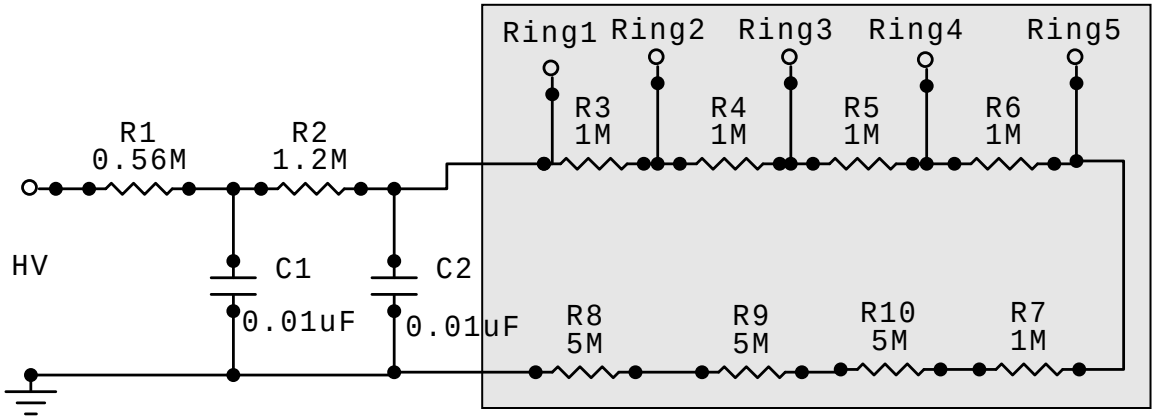

Figure 2.17. High voltage connections. Right: the shaded bow shows the voltage divider. Left: high voltage filter.

The preamplifier output is connected to two Ortec Spectroscopy Amplifiers (model 570), with twenty times gain difference between them. The test pulse was used to verify the gain between the two amplifiers. Each amplifier output is connected to a Multiport Multichannel Analyzer (Multiport II® MCA by Canberra). The Multiport II is fully supported and fully remote-controlled by a portable computer with Genie 2000® software, as shown in Figure 2.18.

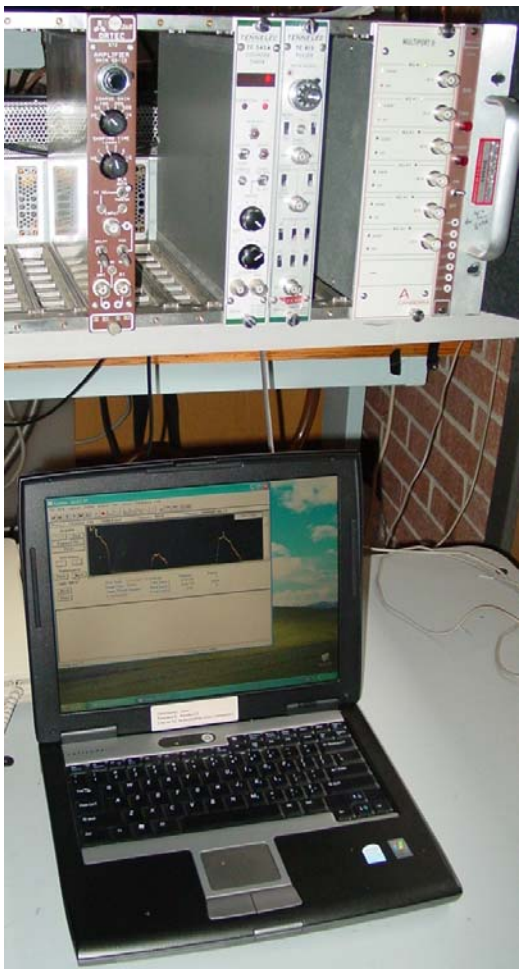

Figure 2.18. Acquisition system. Top: multichannel analyzer, Multiport II. Botton: portable computer with Genie 2000® software.

Since typical energy deposition spectra for high energy particles include events from 0.01 to 1,000 keV/μm, if just one multichannel analyzer is used to record the whole pulse height spectrum, it would need 100,000 channels to provide the needed resolution. It is easier to use two MCAs with 1,024 channels each and separate amplifiers. High gain MCA covers signals from the equivalent of 0 to 1000 electrons with a resolution of 1 electron (0.023 keV) per channel, and low gain MCA covers from 0 to 20,000 electrons with 20 electron (0.46 keV) resolution.

CHAPTER III

DETECTOR TESTING

3.1. Noise

The detector was tested using an Americium-241/Beryllium (AmBe) source which has a half life of 432 yr, 4.4 MeV dose equivalent average energy, and 2.0 x 10^{-19} $Sv.s^{-1}.kg^{-1}$ specific neutron dose-equivalent rate a 1 m distance (Gibson, 1985). The detector was placed 12.5 cm from the neutron source and the spectra were acquired for 14400 seconds. The same procedure was repeated without the neutron source in order to measure the background and electronic noise, as shown in the Figures 3.1 and 3.2.

For convenience when visually inspecting data as it is accumulated, it is important to have the MCA adjusted so that 0 pulse height falls in channel zero. The channel zero adjustment was performed using two different test pulser amplitudes; one twice of the other. The channel number difference corresponding to the maximum of each pulse amplitude spectral peak was set as the channel number for the lowest amplitude pulse peak. The electronic gain difference between the two amplifiers was also verified acquiring the test pulse in both multichannel analyzers. The high gain pulse channel was twenty times the low one.

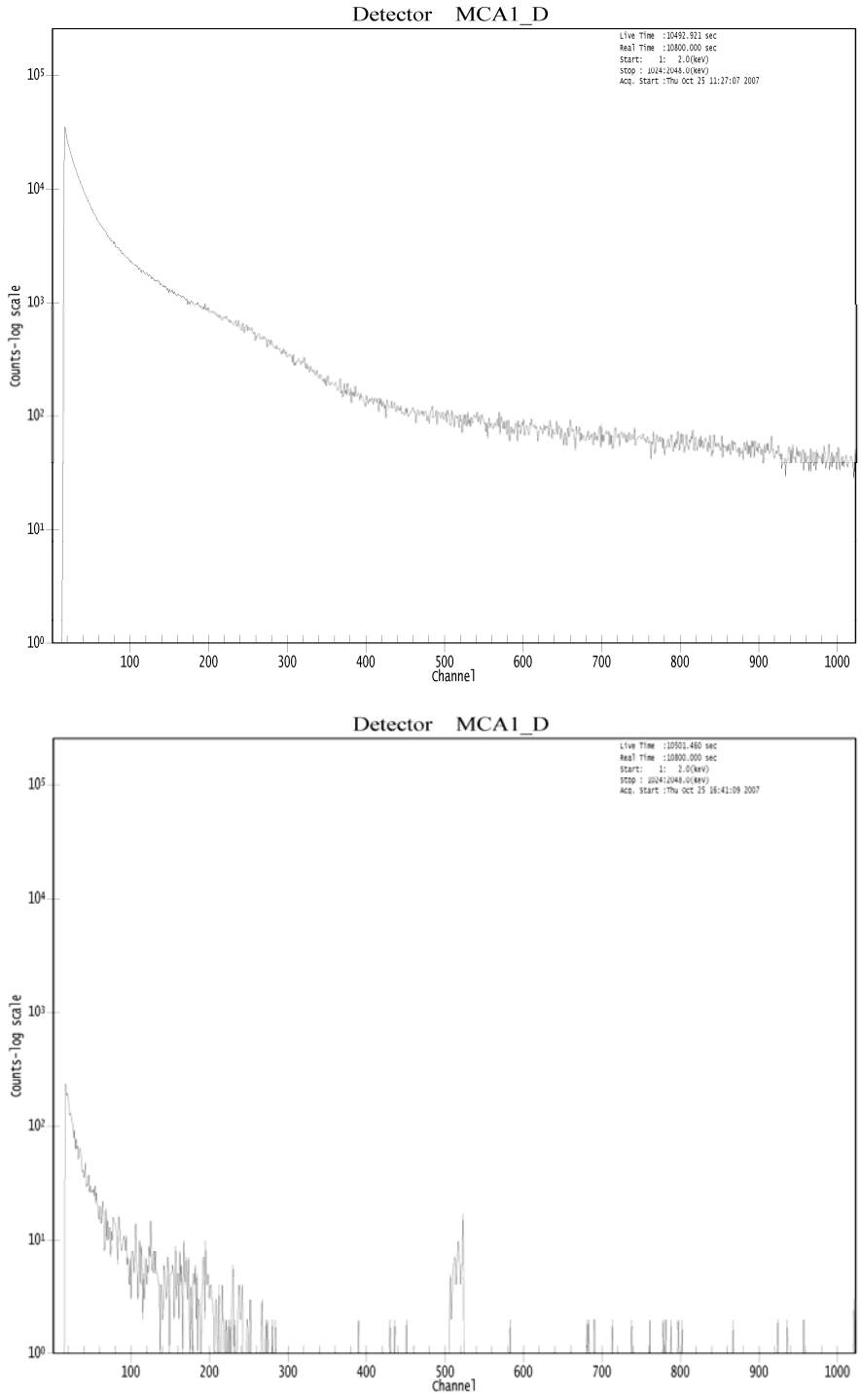

Figure 3.1. High gain raw spectrum. Top: with the AmBe neutron source, bottom: no source present.

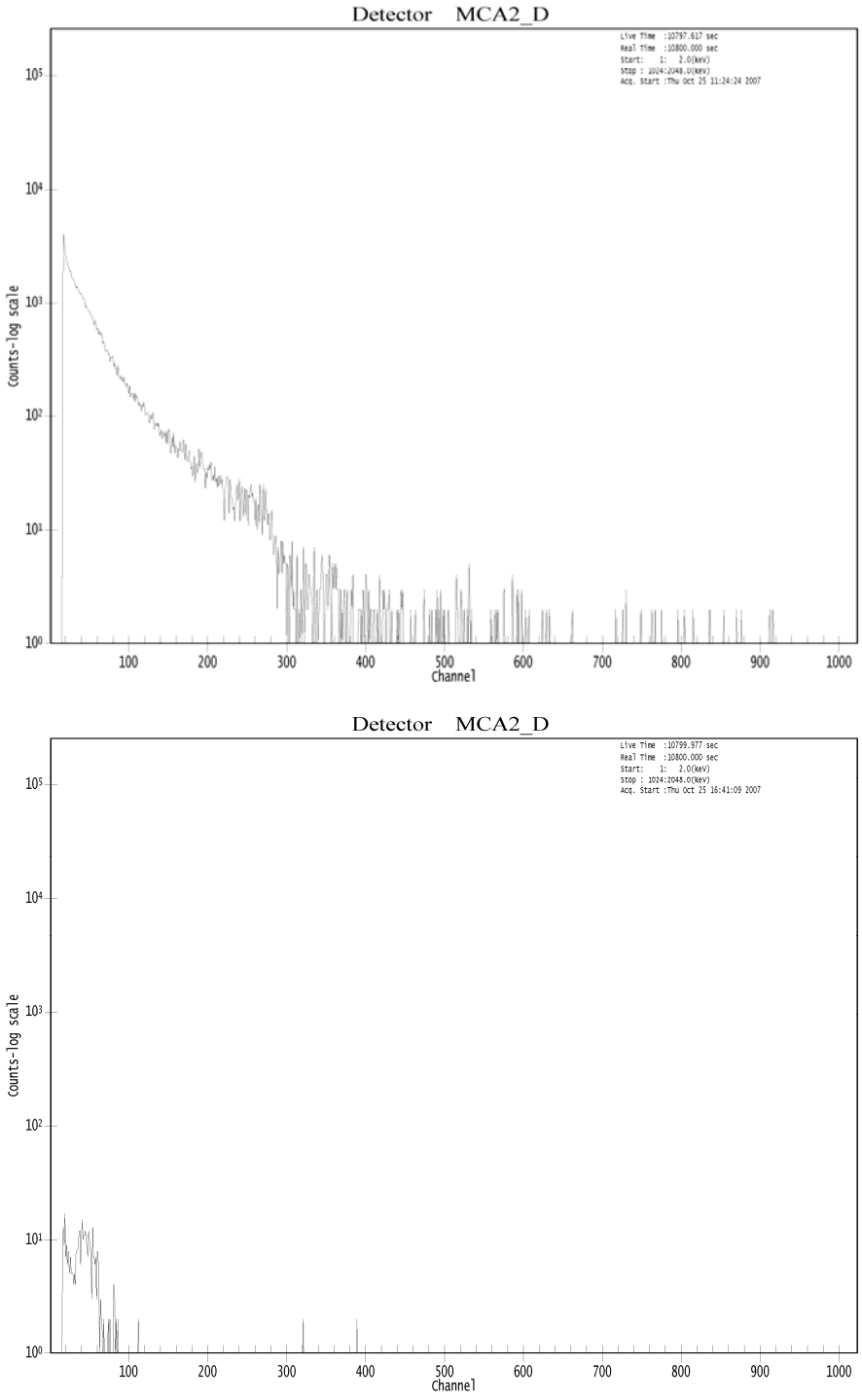

Figure 3.2. Low gain raw spectrum. Top: with neutron source, bottom: with no source present.

The Genie 2000 software also reports counts per channel in text format and portable document format (pdf). The background spectrum was subtracted from the spectrum with the AmBe source, and the data was processed using microdosimetry standard procedures. To initiate a new spectrum acquisition the software has to be restarted in order to obtain a new data report. Otherwise, the software will keep the information of the previous acquisition when the reset option is used.

3.2. Gas Gain

The gas gain as a function of applied voltage is an important characteristic of the detector. In order to evaluate the gas gain it is necessary to determine the electronic system characteristics. Using a known test pulse amplitude V_t on the test capacitor C_t, the charge delivered to the preamplifier input is given by

$$q = V_t \cdot C_t, \tag{3.1}$$

the number of electrons is calculated as

$$\#\,\text{of electrons} = \frac{q}{e} = \frac{V_t C_t}{e}, \tag{3.2}$$

where e is the electron charge. The mean channel number for a specified test pulse voltage was determined and used to calculated the number of electrons per channel at the preamplifier input using

$$\#\ \text{of electrons per channel} = \frac{V_t C_t}{e \cdot \text{channel number}}. \qquad 3.3$$

Using the same MCA and shaping amplifier settings to record the spectrum produced by the detector being exposed to an AmBe source, a visual inspection of the spectrum reveals the proton drop point channel, the midpoint of the region of the greatest negative slope in the energy deposition spectrum, as shown in Figure 3.3.

Theoretically, the proton drop point corresponds to the maximum energy deposited by proton for the maximum chord length in the detector. In tissue the maximum LET of proton is about 100 keV/μm. The energy imparted in a detector simulating 2μm diameter spherical site is calculated as

$$\varepsilon = 2\ \mu\text{m} \times 100\ \text{keV}/\mu\text{m} = 200\ \text{keV}. \qquad 3.4$$

The gas gain is given by

$$\text{Gas Gain} = \frac{\#\ \text{of electrons per channel} \bullet \text{Proton Drop Point channel}}{\varepsilon / \omega}, \qquad 3.5$$

where ω is mean energy per ion pair.

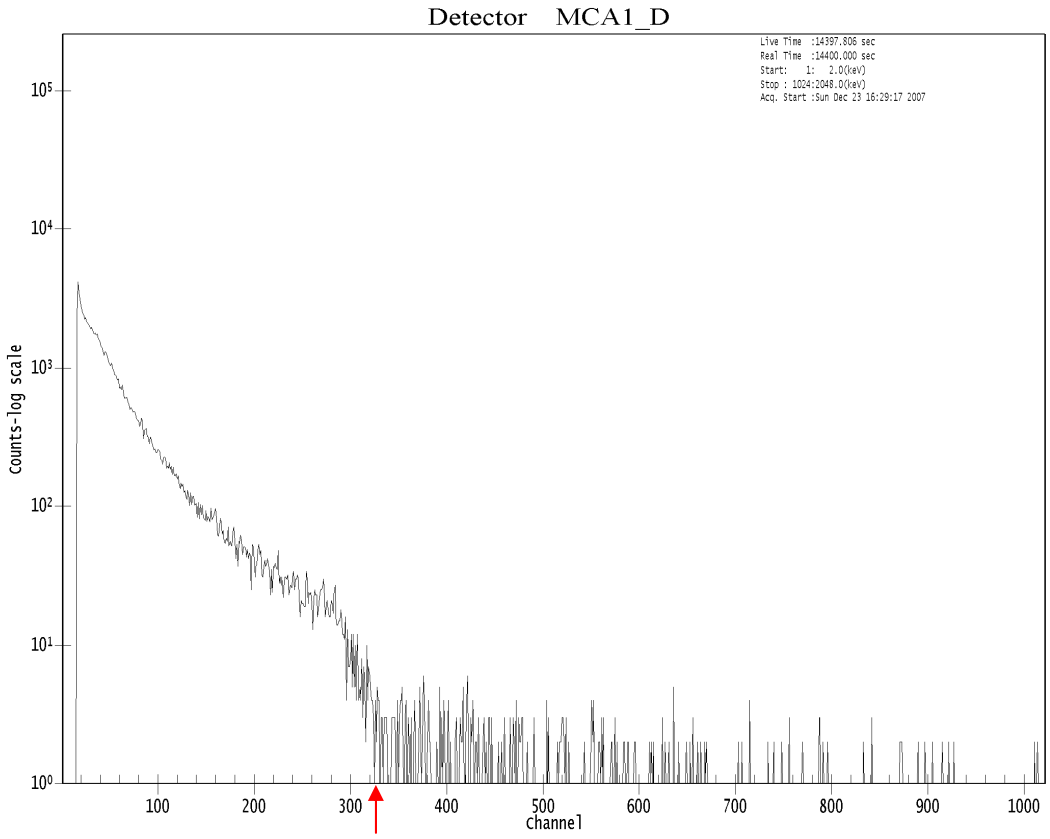

Figure 3.3. Low gain spectrum. The red arrow indicates the proton drop point in this spectrum around channel 325.

Energy calibration is achieved using the following linear relationships

$$y = \frac{\varepsilon}{\bar{l}}, \tag{3.6}$$

where $\bar{l}$ is the mean chord length, and for a spherical detector is 2d/3, then the calibration factor is given by

$$\text{Calibration factor} = \frac{y}{\text{Proton Drop Point channel}}. \qquad 3.7$$

Low gain spectra were acquired using source voltage from 550 V to 850 V at 50 V intervals. Using the proton drop point, the gas gain was calculated using the equations described above. For example, when the pulse voltage was 32 mV with a test capacitor capacitance of 0.4 pF, the shaping amplifier gains were the 1 and 20, and MCA gain was 1024 channels per 5 V, the MCA recorded the test pulse maximum in channel 18.5. The number of electrons per channel in this case is 4,444.

The gas gain was calculated using $\bar{\omega}$ for propane of 26.2 eV (ICRU Report 31), the energy imparted of 200 keV, and the number of electrons per channel. The table 3.1 shows the proton drop point for different detector voltages, and the calibration for each spectrum.

The $\bar{\omega}$ value used to calculate the gas gain in this detector from ICRU Report 31 is the $\bar{\omega}$ value for 5.3 MeV alpha particles in propane. There is no proton experimental data available for propane in ICRU report 31, but they suggest using the $\bar{\omega}$ value for 5.3 MeV alpha particles in those gasses where the protons have energies over 0.1 MeV.

Table 3.1. Proton drop point for different detector voltages.

Detector Voltage (V)	Proton Drop Point (Channel number)	Calibration (keV/μm per channel)
506	39.5	3.86
552	61.5	2.44
598	113.5	1.54
644	177.5	0.85
690	265.5	0.56
736	473.5	0.32
782	825.5	0.17

The gas gain was calculated for each voltage and represented as a function of the detector voltage. Figure 3.4 shows an exponential trendline with 0.0101 decay rate constant and amplitude of 0.0969. There is approximately a factor of 1.6 gas gain increment for each 50 V increase in the anode potential.

Figure 3.4 also shows gas gain for different voltages for Rossi style counters, anode and cathode dimensions. They are spherical TEPCs using propane based tissue equivalent gas some of them with grid and other with field correction pieces (Srdoc, 1970). The trendline is very similar; all of them have an exponential behavior. For this detector in particular, the propane gas gain should not exceed the 1,000 electrons because for high

LET radiation the gas will not have a linear behavior. Srdoc was using a very high gas gain because his detector was used for x-rays.

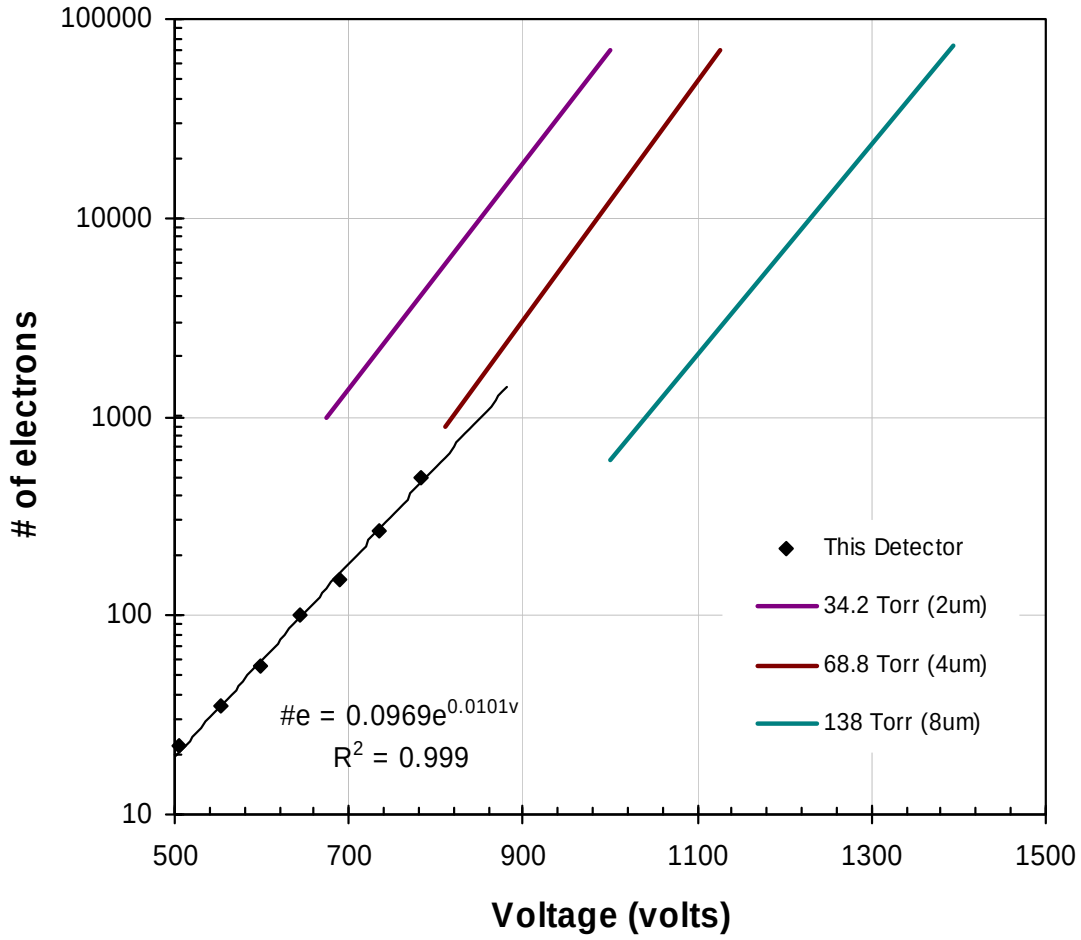

Figure 3.4. Gas gain as a function of detector's voltage. The gas gain was calculated for voltage between 550 V and 850 V for this detector (black diamonds). Solid lines are gain curves for spherical detectors of different design simulating 2 to 8 µm diameter sites (adapted from Srdoc, 1970).

In order to plot the probability density function f(y), the data from the two MCAs were merged into a single, continuous spectrum for each detector voltage. The high gain spectra were recalibrated multiplying each channel number by 1/20. To correct for differences in counts due to differences in dead time, the counts from channel 20 of the low gain spectrum were divided by the sum of the counts from channels 390 to 410 from high gain spectrum. The counts in each channel of the high gain spectrum were multiplied by the resulting factor.

In order to illustrate the full range of energy depositions produce by a mixed radiation environment is customary to plot $y^2f(y)$ versus the log of y. The area under this curve is proportional to the dose in an interval of y. The methods for preparing these plots are given in appendix A.

Figure 3.5 shows the spectrum after the procedure described in Appendix A. This spectrum corresponds to a spherical detector simulating a 2μm size site at 750 V. The first peak represents the gamma events, the second is the neutrons events, and the last one is the carbon ions and alpha particles. Also around channel 265.5 is the proton drop point. The calibration for this gas gain was 0.56 keV/μm per channel, and the lowest most value energy was 0.4 keV/μm. The highest voltage applied was 850 V; it could not be increased further with the electronics used because the amplifier gain could not be reduced further and the proton drop point at higher voltage would be out the scale.

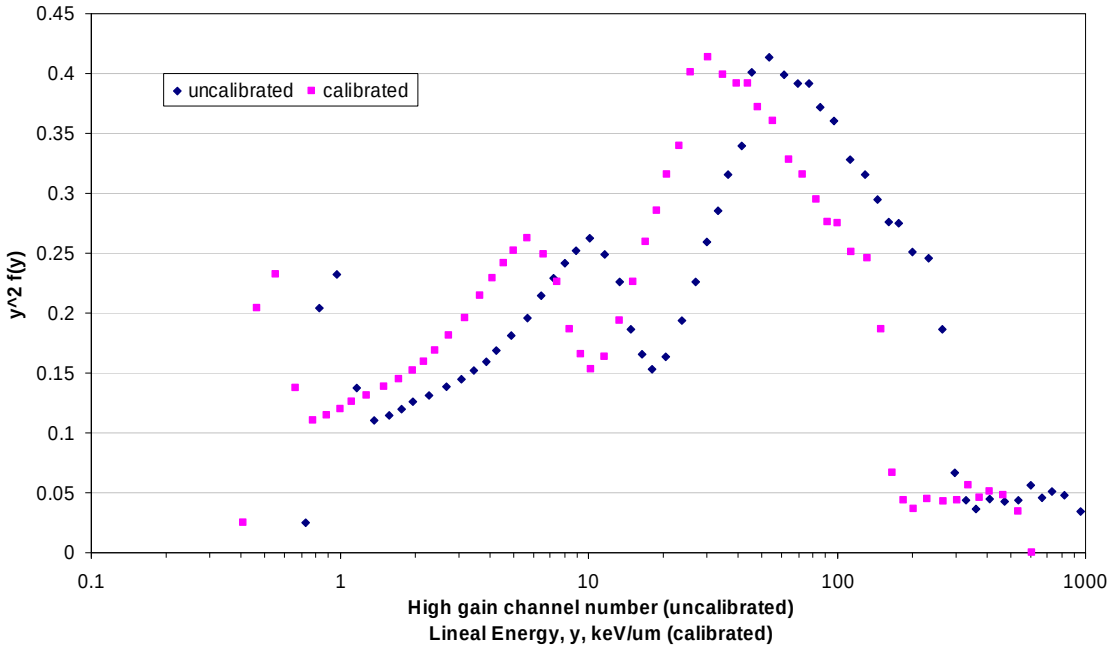

Figure 3.5. Typical microdosimetry spectrum representation. Detector exposed to an AmBe neutron source for 14400 sec.

CHAPTER IV

DETECTOR IMPLEMENTATION

4.1. Angular Response

In order to estimate the detector angular response a group of spectra were acquired for different angles. The center of the TE shell was marked on the outside of the stainless steel detector container. The detector center was placed coincident with the center of a 12.5 cm circle. To avoid unnecessary off-centering, the detector was attached to a piece of wood by two stainless steel clamp bands. For these experiments an AmBe neutron source was used. Data acquisition at different sensor-source angles were made using an acquisition time of 14,400 s and a detector bias voltage of 850 V. Figure 4.1 shows the detector position and the angles used to see the response.

The spectra were collected for the source at 0^o, 45^o, 90^o, 135^o, 180^o, 225^o, and 335^o relative to a line through the center of the detector perpendicular to the anode. Then, the detector was rotated 90^o about its main axis of symmetry and the spectra were collected again for the same angles. Due to the detector electrical connections it was physically impossible to place the source at 270^o angle.

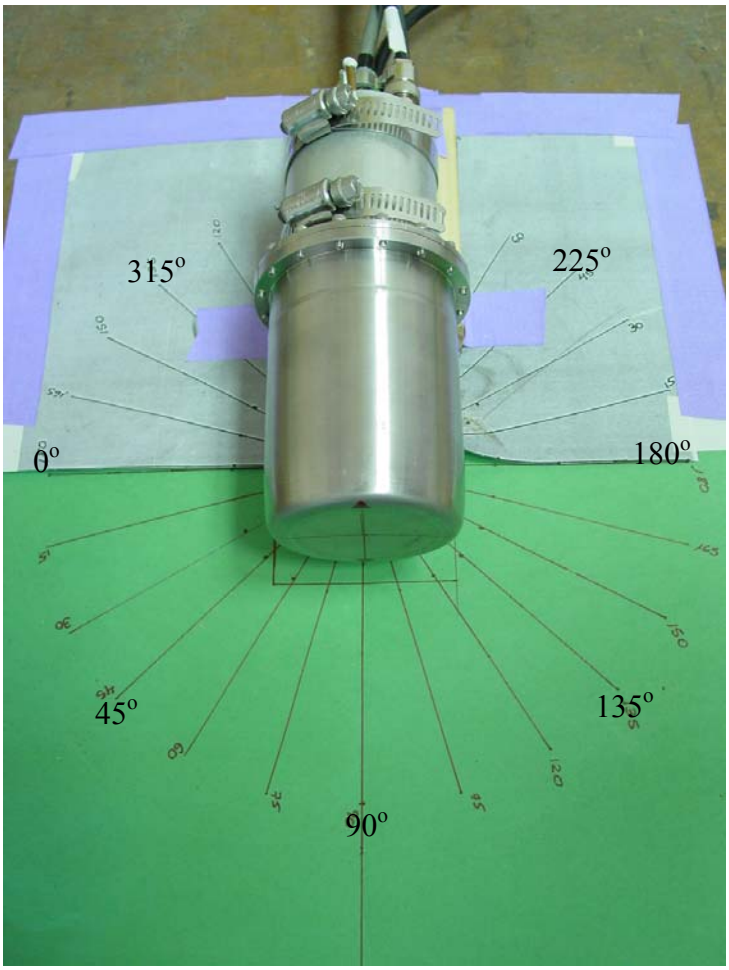

Figure 4.1. Geometrical arrangement for angular response. A spectrum was acquired for several sensor-source angles.

The plots of the obtained spectra *yf(y)* for different sensor-source angles are shown in Figure 4.2. It is evident that the main features of the spectrum, such as peaks, and proton drop-points appear consistently at the same channel numbers with small differences in amplitude. In order to analyze quantitatively the resulting spectra it is better to calculate the absorbed dose for each angle. The dose was calculated as:

$$D = \frac{1}{m}\left(\sum Ny\right) * \text{calibration factor}, \tag{4.1}$$

where N is the number of counts, y is the channel number, and m is the simulated site mass. The calibration factor, given by the Equation 3.7, was calculated as 0.3663 for these spectra.

In order to calculate the mass, the volume was calculated using the sphere equation with the simulated size site data

$$V = \frac{\pi d^3}{6}, \tag{4.2}$$

where d is 2 μm. Using the tissue density 1 g/cm^3, the mass is given by

$$m = \rho V\left(\frac{d_g}{d_{ss}}\right)^2, \tag{4.3}$$

where d_{ss} is the simulated size site diameter. The calculated mass for this detector is 0.34 μg.

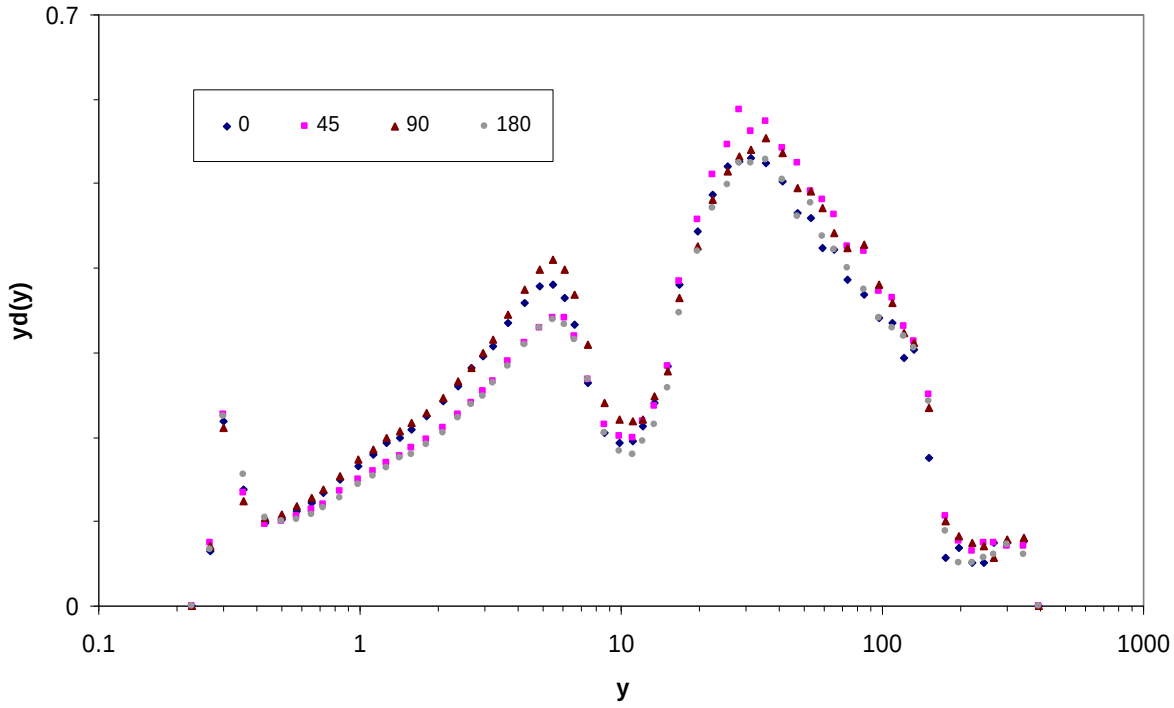

Figure 4.2. Detector angular response. Right peak is produced by photons interactions; left peak is produce by protons interactions.

Besides neutrons, the AmBe source also produces in 42.7% of the times 13.9 keV gamma rays (see Appendix B). For practical reasons the absorbed dose was calculated for energies over 10 keV (proton's peak), and under 10 keV (photon's peak) separately. This was done because detector is intended for space dosimetry where the predominant radiation type is high energy charged particles, and the low energy photons will not be playing any role. Table 4.1 shows the absorbed dose for energies over 10 keV. Absorbed doses with high relative errors were calculated using spectra acquired during working hours.

Table 4.1. Calculated absorbed dose for energies over 10 keV.

Angle	Energy (keV)	Relative Error	Dose (Gy)
0^o	2615842	0.0%	1.24E-03
45^o	2370815	9.4%	1.12E-03
90^o	2562986	2.0%	1.22E-03
135^o	2680913	2.5%	1.27E-03
180^o	2713038	3.7%	1.29E-03
225^o	2882490	10.2%	1.37E-03
315^o	2510927	4.0%	1.19E-03
After Rotation			
0^o	2526057	3.4%	1.20E-03
45^o	2454574	6.2%	1.16E-03
90^o	2540862	2.9%	1.20E-03
135^o	2330256	10.9%	1.11E-03
180^o	2799284	7.0%	1.33E-03
225^o	2660298	1.7%	1.26E-03
315^o	2618102	0.1%	1.24E-03

The relative error for the absorbed dose due to events over 10 keV was, in 9 out 14, angles lower than 5%. The remaining dose calculations were less than 10%. Some of the spectra were acquired during working hours, which could have increased the radiation

background due to the Texas A&M University Nuclear Science Center nuclear reactor running during the acquisition. This increment in the background intensity was noticed after the 180^{o} experiment was measured twice; during the Nuclear Science Center (NSC) work hours and during the night. The resulting raw spectra, at first glance, look almost the same (see Figures 4.3 and 4.4) but after calculating the dose for each case, the absorbed dose during work hours was 1.45 mGy while during night time was 1.29 mGy. Figure 4.5 shows the two 180^{o} spectra overlayed for the reader to assess the differences.

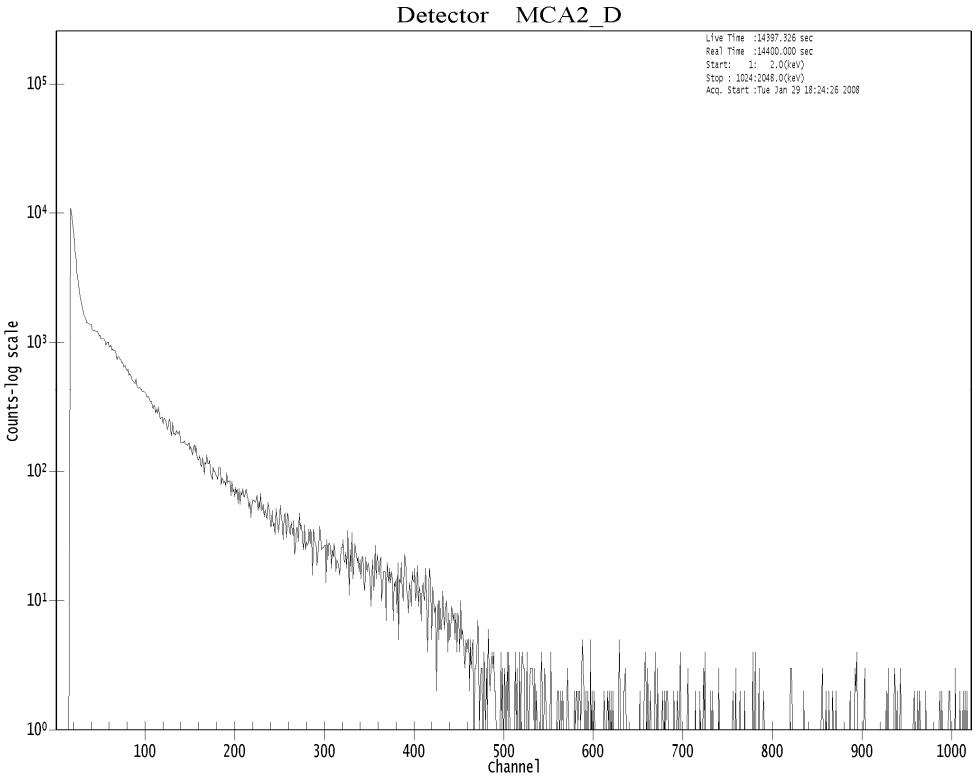

Figure 4.3. Low gain raw spectrum at 180^{o} at day time. Acquisition during NSC work hours.

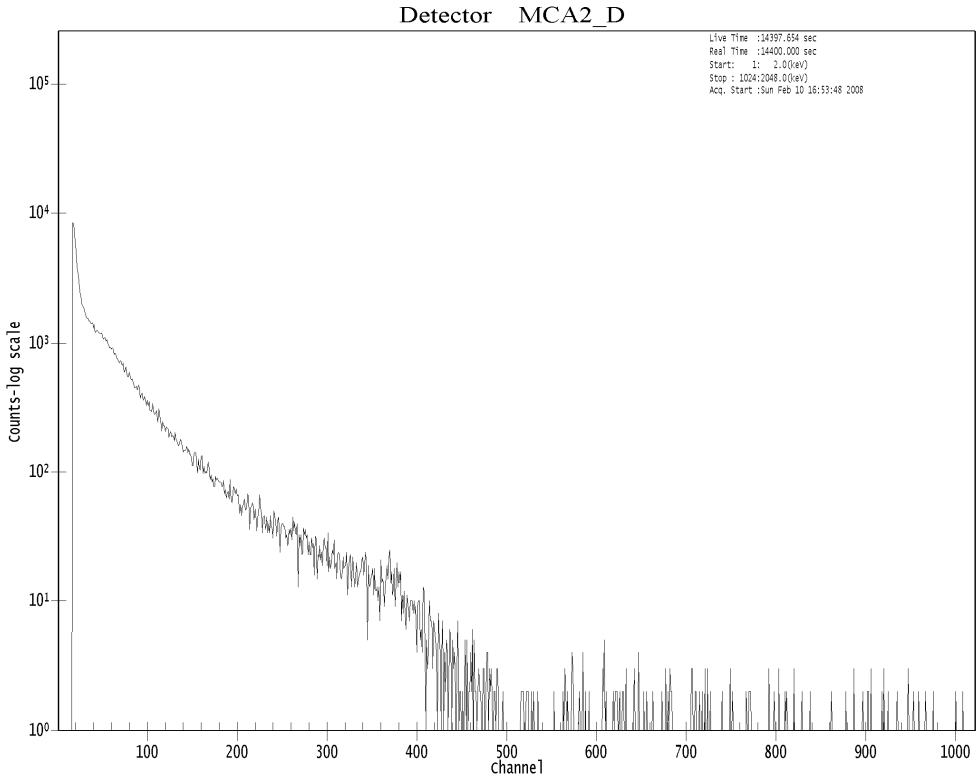

Figure 4.4. Low gain raw spectrum at 180^{o} at night time. Acquisition during night hours.

The relative error for the absorbed dose under 10 keV was in all the cases more than 8%. The spectra acquired during work hours shows an evident difference from the ones acquired during night time, even evident by inspecting the raw spectra. In the 135^{o} case, the absorbed dose varied from 2.5 mGy during work hours to 0.5 mGy during night time. The radiation background is very likely to increase because of the research nuclear reactor running during the acquisition, but the electronic noise may also change between work hours and night time, contributing to spectra variations. Figure 4.6 shows the resulting 135^{o} case spectra during work hours and after hours. In this case, there is a very

large difference. In the spectra the night spectrum, the trend line is a continuous decay, but the daytime spectrum shows a plateau between channels 20 to 100.

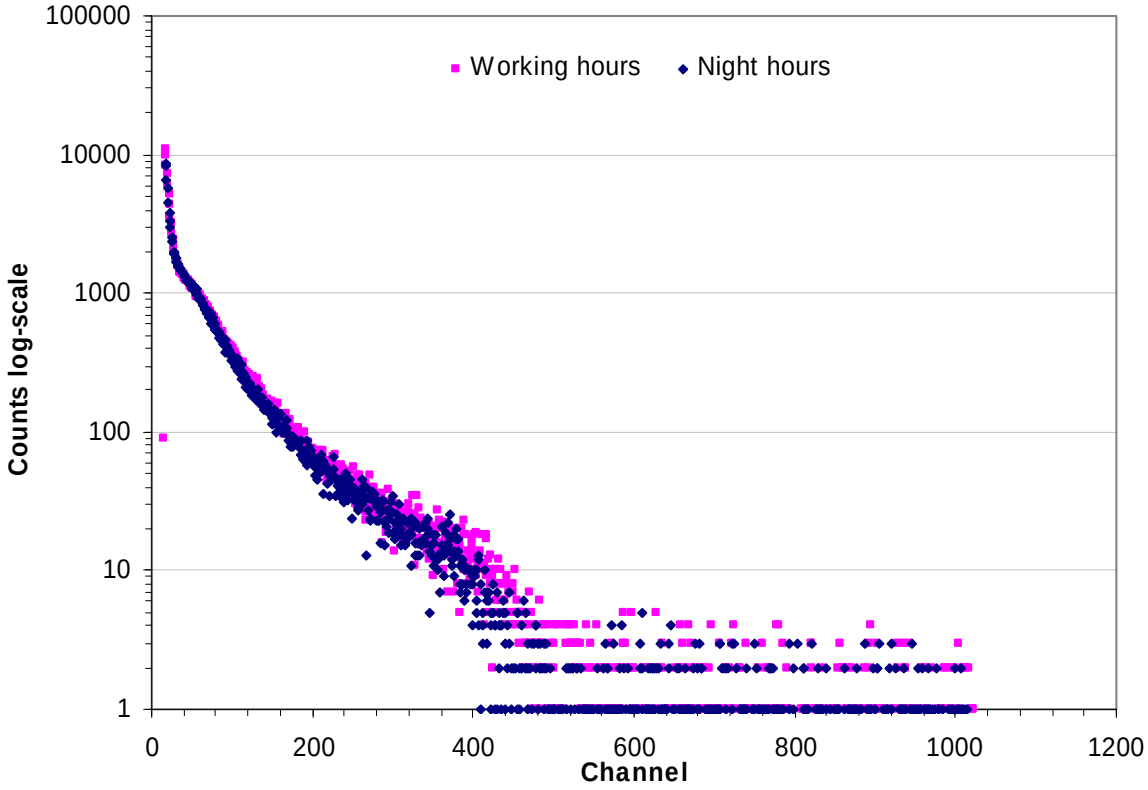

Figure 4.5. Low gain spectra at 180°. Pink squares: work hours; blue diamonds: night hours.

Table 4.2 shows the absorbed dose for energies under 10 keV. The absorbed dose relative error was higher than for energies over 10 keV. This may be attributed to a higher electronic noise on this part of the spectrum.

Table 4.2. Calculated absorbed dose for energies under 10 keV.

Angle	Energy (keV)	Relative Error	Dose (Gy)
0^o	1591766.4	0.0%	7.55E-04
45^o	1260268	20.8%	5.98E-04
90^o	2020412	26.9%	9.58E-04
135^o	1739980	9.3%	8.25E-04
180^o	1789932	12.4%	8.49E-04
225^o	1110965	30.2%	5.27E-04
315^o	3716096	133.5%	1.76E-03
After Rotation			
0^o	1772150	11.3%	8.40E-04
45^o	1453840	8.7%	6.89E-04
90^o	1771669	11.3%	8.40E-04
135^o	1054089	33.8%	5.00E-04
180^o	1792254	12.6%	8.50E-04
225^o	959641	39.7%	4.55E-04
315^o	940028.8	40.9%	4.46E-04

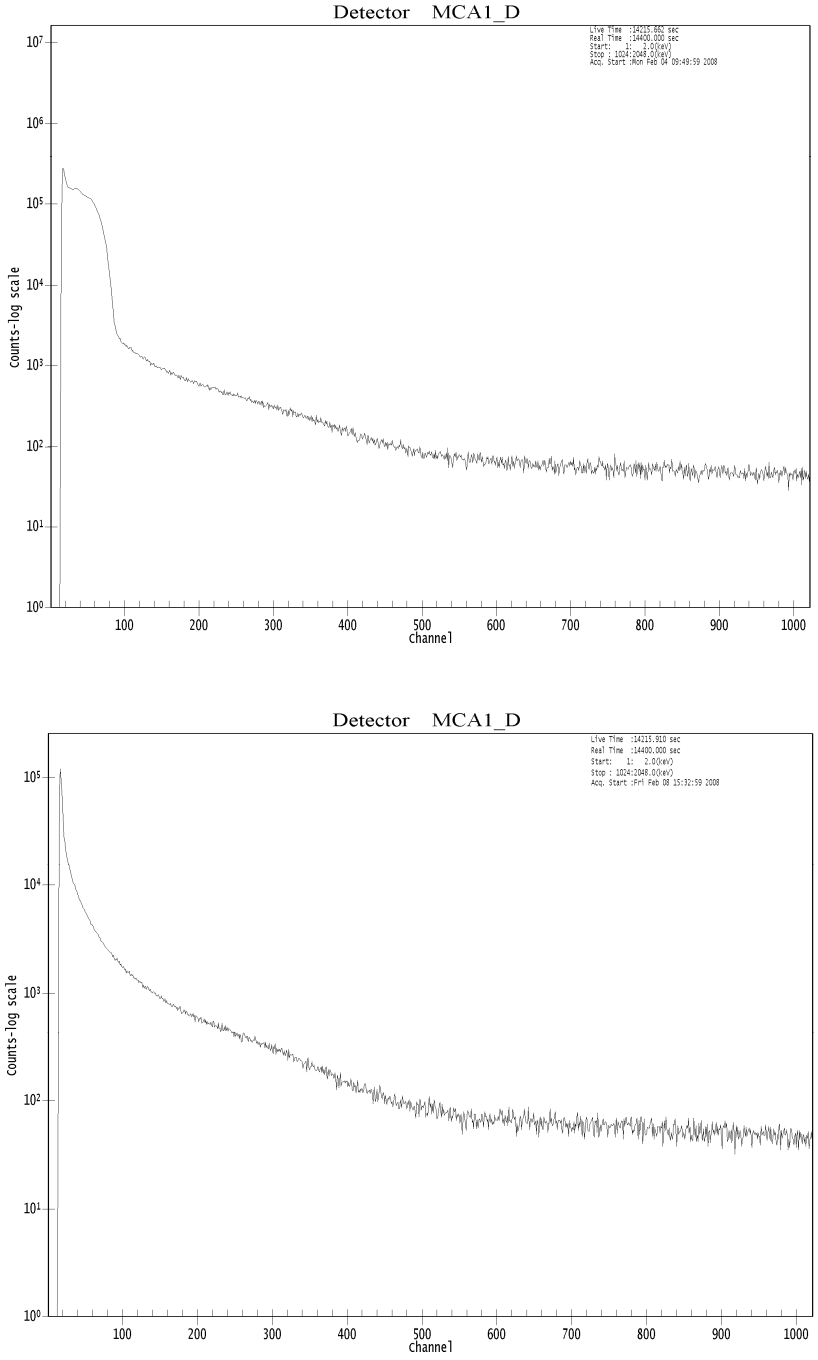

Figure 4.6. High gain spectra at 135^{o}. Top: acquisition during NSC work hours; bottom: acquisition during night time.

Although the photon component is not critical, it may be feasible to decrease the relative error to less than 10% doing all the acquisition during weekends and night, and also changing the geographical location of the experiments. Due to the drastic changes in the spectra, it is possible that the proton dose error may decrease considerable, to under 5% for all the angles. One important experimental result is that by repeating the spectra for the same angle and under very similar background conditions, there is a statistical error of approximately 3%.

4.2. Neutron Drop Point Resolution

The spectrum *yd(y)* can be interpreted as the envelope of a continuum of Gaussian distributions, each one represent a monoenergetic proton spectrum:

$$f(y_i, \mathbf{b}) = \sum_{j=1}^{\infty} \alpha_j \exp\left[-\frac{(y_i - y_{0j})^2}{2\sigma_j^2} \right] + \alpha , \qquad 4.4$$

where the set of parameters **b** = (α_j, x_{0j}, σ_j, α) define the amplitudes α_j, Gaussian centers y_{0j}, Gaussian widths σ_j, and background level α. The spectral function *f* is also a function of the channel number or energy *y*.

Determination of the proton drop-point is valuable for computing the gas gain and resolution of the TEPC. The energy at which the proton drop point occurs in the

spectrum has an uncertainty due to MCA sampling interval and the sensor resolution. Visual estimation of the inflection point at the proton drop point gives rise to a good estimate. Also, it can be estimated by fitting a superposition of a finite number of Gaussians to a subset of the spectrum *f* that contains the proton drop point.

Fitting the model described by equation (4.4) to a subset $\boldsymbol{d} = (d_1, d_2, \ldots d_i)^T$ of the spectrum f is achieved by solving the problem $\mathbf{b}^* = \text{argmin}(S(\mathbf{b}))$ under the constraint that both amplitudes α_j, widths σ_j, and background level α_5 must be positive. The cost function:

$$S(\mathbf{b}) = \frac{1}{2}\|\mathbf{F}(\mathbf{b})\|_2^2, \tag{4.5}$$

is the Euclidean norm of the weighted residuals

$$F_i(\mathbf{b}) = \frac{d_i - f(\mathbf{x}_i, \mathbf{b})}{f(\mathbf{x}_i, \mathbf{b})}. \tag{4.6}$$

Equations (4.4) through (4.6) correspond to a non-linear weighted least squares optimization problem. The smooth behavior of the spectrum and the physical nature of the proton drop point enable us to simplify the model given by Equation (4.4). First, a few Gaussian functions at predetermined locations can be used to fit the spectrum data. Second, the center of one of the Gaussians is fixed at the energy (or channel number)

corresponding to the point located just before of the region of the greatest negative slope in the energy deposition spectrum. At energies higher than the proton drop point, no more Gaussians contribute to the spectra but some background noise that can be modeled by a constant value α.

The non-linear least squares problem was solved using the Generalized Reduced Gradient (GRG2) (Lasdon and Waren, 1979), algorithm that also can be found as the add-in solver on Microsoft Excel. Using 19 data points corresponding to spectral values between channel 85.5 and 729.5, a good minimization of the cost function (4.5) was found by using four Gaussians (5.9 % of misfit). The minimization is achieved after a few tens of iterations. An example of the "best" Gaussians and background noise modeled by the optimized model $\mathbf{b}^*$ and its corresponding superposition is shown in Figure 4.7.

From the width σ_4 of the fitted Gaussian at the drop point, the proton drop point is calculated as $x_{o4} + 0.5\sigma_4$. The standard deviation for the interested Gaussian is 30.36, and the full width at half maximum is:

$$\text{FWHM}=2.35\sigma^*\text{calibration factor}, \qquad 4.7$$

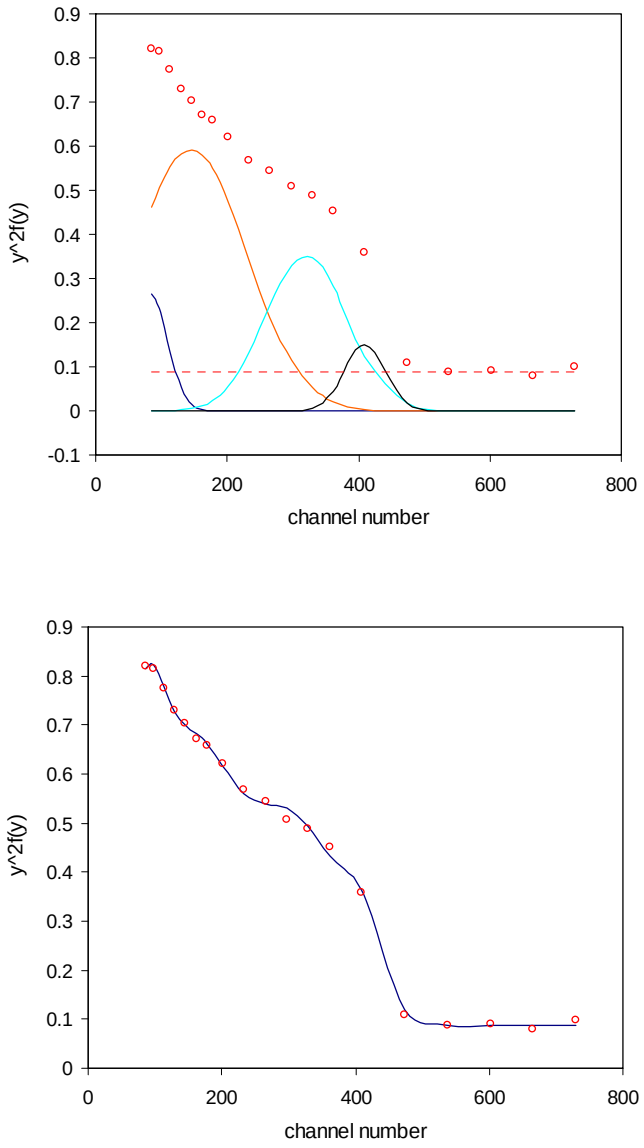

Figure 4.7. Multi-Gaussian fitting for modeling the proton drop point. Red circles represent the spectral data. Top: colored lines the Gaussians and background noise resulting from the non-linear optimization. Notice that one of the Gaussians (Black line) is centered on the proton drop point. Bottom: The superposition of the best-fit functions shows that the whole spectrum subset and the drop point are properly modeled.

Using the optimum model parameters, the FWHM value of 26.13 keV/μm or 17.4% was found for the TEPC detector. Using the procedure described above with 1.5 MeV neutron data from a 2 μm site size wall-less detector (Rossi, 1996) the standard deviation with the calibration factor was 11.3, and the FWHM value of 26.55 keV/μ or 17.7 %. The resolution for this detector is similar to the resolution of other high performance proportional counters.

CHAPTER V

CONCLUSIONS AND RECOMMENDATIONS

In this work a new spherical TEPC was designed, constructed and tested. Numerical simulations using Monte Carlo Method provided an estimate of corrections needed if charge particle equilibrium for the protons produce by high energy neutrons is not possible.

When compared with similar, high performance proportional counters such as those used by Srdoc, the new TEPC provides low electronic noise, similar relationship between gas gain values and the detector voltage, good spectral resolution (26.13 keV/μm), excellent isotropic angular response (only 7% variation), and a smaller detector size (1.778 cm internal diameter, 0.5 cm wall thickness). The experimental performance along with its size makes it suitable for spacecraft dosimetry.

Further refinements on detector construction and electronic circuitry optimization would lead to improvements on sensor performance, size reduction, and reliability. A look back to the road followed during this research makes clear a few suggestions that would help to provide an even better TEPC.

Regarding the detector construction, molds should be made out of stainless steel to minimize "sticking" of the molten plastic against the metal, reduce the mold bending in

the case of the thinner mold parts, and allow a slower cooling of the hemispherical shell segments. Also, improved cutting tools used to form the polyethylene insulating layers would minimize production of wedges or whiskers of polyethylene on the inside of the detector that can accumulate charge, distorting the electric field homogeneity. The electric connections to each of the rings should be improved by reducing wire gauge, and using Gold-covered wire which can be easily welded to the voltage divider.

In regards to the electronics, the preamplifier board should be re-designed to provide a more compact circuit, saving space inside the detector's gas container. Gold-covered wiring, on-board connectors and placing the preamplifier board at one of the sphere "poles" would improve the detector response. The same applies to the voltage divider board; both miniaturization and improve board design is advisable. It would be interesting to integrate the input NJFET gate to the ceramic standoff that serves as the feedback capacitor using a surface mount component. The use of low dielectric constant circuit boards would reduce the influence of unwanted, distributed capacitances.

Finally, in order to reduce the amount of time required for sensor testing experiments, it would be important to assess the possibility to improve the sensor testing facility particularly reducing background radiation.

REFERENCES

American Association of Physicist in Medicine. Protocol for neutron beam Dosimetry. New York. AAPM Report No. 7; 1980.

Bailey V. Radiation protection and instrumentation. In: Biomedical results of Apollo. [online book]. Section II, Chapter 3; 1975. Available at: http://lsda.jsc.nasa.gov/books/apollo/S2ch3.htm. Accessed 21 February 2008.

Belonogii PN, Drobchenko EA. Spherical tissue equivalent proportional counter with coaxial electric field. Meas Tech+ 10: 901-903; 1985.

Benjamin PW, Kemshall CD, Redfearn J. A high resolution spherical proportional counter. Nucl Instrum Methods 59: 77-85; 1968.

Braby LA, Johnson GW, Barthe J. Practical considerations in the design and construction if tissue-equivalent proportional counters. Radiat Prot Dosim 61: 351-379; 1995.

Gibson JA, Piesch E. Neutron monitoring for radiological protection. Vienna, Technical Reports Series No. 252 IAEA; 1985.

Goodman LJ. Density and composition uniformity of A-150 tissue-equivalent plastic. Phys Med Biol 23: 753-758; 1978.

Guetersloh SB, Borak TB, Taddei PJ, Zeitlin C, Heilbronn L, Miller J, Murakami T, Iwata Y. The response of a spherical tissue-equivalent proportional counter to different ions having similar linear energy transfer. Radiat Res 161: 64-71; 2004.

International Commission on Radiation Units and Measurements, Inc. Average energy required to produce an ion pair. Washington, D.C. ICRU Report 31; 1979.

International Commission on Radiation Units and Measurements, Inc. Fundamental quantities and units for ionizing radiation. Washington, D.C. ICRU Report 60; 1998.

Kastner J, Oltman BG, Feige Y, Gold R. Neutron exposure to lunar astronauts. Health Phys 17: 732-733; 1969.

Lasdon LS, Waren AD. Generalized reduced gradient software for linearly and nonlinearly constrained problems. In: Greenberg HJ, editor. Design and implementation of optimization software. The Netherlands: Sijthoff and Noordhoff Publishers; 1979.

Rossi HH, Zaider M. Microdosimetry and its applications. New York: Springer-Verlag; 1996.

Sandmeyer Steel Company. Alloy 303. [online]. Available at: http://www.sandmeyersteel.com/images/303-spec-sheet.pdf. Accessed 21 Feb 2008.

Space Radiation Analysis Group (SRAG). Johnson Space Center. NASA [online]. Available at: http://srag.jsc.nasa.gov. Accessed 18 Feb 2008.

Srdoc D. Experimental technique of measurement of microscopic energy distribution in irradiated matter using Rossi counters. Rad Res 43: 302-319; 1970.

Turner JE. Atoms, radiation, and radiation protection. 2nd ed. New York: Wiley & Sons; 1995.

APPENDIX A

GRAPHICAL PRESENTATION OF DATA

Using a linear representation, the details of the distribution are not visible. The log-log representation will enhance the significance of the small events, compressing the relative amplitude of large events. The semi-log is the most common representation for the frequency of events f(y)

$$f(y) = \frac{N(y)}{\sum_i N_i(y)}, \qquad \text{A.1}$$

where f(y) is the normalized number of events. To illustrate the contribution of different size events to the dose, it is better to plot the probability density of dose, designated d(y)

$$d(y) = y f(y), \qquad \text{A.2}$$

but to plot the probability density of dose vs. log y we need to use (Rossi and Zaider, 1996)

$$y d(y) = y^2 f(y) \qquad \text{A.3}$$

Large events are typically rare, and data above 150 keV/μm often have a few channels with one count and many with zero. Results could be plotted as yf(y) or yd(y) vs. log y

point by point, but this would lead to strange fan-shaped plots that are hard to interpret. It is better to average data in progressively wider bins as the value of y increases. This is done by adding counts in a group of channels and dividing by the new bin width to get average n(y) in a region.

The new bin width was created using Excel Indirect Addressing Function. A loop was written to create a list of new bins that start at MCA channel (Ga,b) and end (Ha,b), where a is the current line number and b is the page. Then

SUM(INDIRECT(ADDRESS(Ga,b)):INDIRECT(ADDRESS(Ha,b))) A.4

will give the count summed over those MCA channels. This will end up with 45 bins, each with a calculated mean lineal energy and bin width. The first 19 new bins in the low gain spectrum were substituted by the 45 new bins from the high gain spectrum.

The bins were created using the follow expression

2^(INT(Aa/6)), A.5

making the first 6 bins one channel wide, the next six 2 channels wide, and the third group 4 channels wide.

APPENDIX B

AMERICIUM-241/ BERYLLIUM DATA SHEET

Part 1 – Radioactive Material Identification

Common Names: Americium-241/Beryllium **Chemical Symbol:** Am-241/Be or ^{2}

Atomic Number: 95 **Mass Number:** 241(146 neutrons)

Americium oxide with beryllium metal

Compacted mixture of Americium oxide with beryllium metal

Part 2 – Radiation Characteristics

Physical half-life: 432.2 years **Specific Activity (GBq/g):** 127

Principle Emissions	E_{Max} (keV)	E_{eff} (keV)	Dose Rate (μSv/h/GBq at 1m)	Shielding Required
Beta* (β)	-	-	-	-
Gamma (γ) / X-Rays	13.9 (42.7%) 59.5 (35.9%)	-	85[a]	HVL Lead: 0.01 cm
Alpha (α)	5,443 (12.8%) 5,486 (85.2%)	-	-	-
Neutron (n)	-	4,500	2[a]	HVL Paraffin Wax: 6.6 cm

Where Beta radiation is present, Bremsstrahlung radiation will be produced. Shielding may be required. Note: Only emissions with abundance greater than 10% are shown. [a] *The Health Physics and Radiological Health Handbook,* Scintra, Inc., Revised Edition, 1992

Progeny: Neptunium-237(Np-237)

VITA

Name:	Delia Perez Nunez
Office Address:	Texas A&M University. Department of Nuclear Engineering, mail stop 3133 College Station, TX. 77843.
Office Phone:	(979) 458-0598.
e-mail:	deperez@tamu.edu

B.S., Physics, Universidad Central de Venezuela, Caracas, Nov. 1998

Ph.D., Nuclear Engineering, Texas A & M University, May 2008

Specialization in Instrumentation, Universidad Central de Venezuela, Caracas.

Lic. in Physics, Universidad Central de Venezuela, Caracas.